

Astraeus VIII: A new framework for Lyman- α emitters applied to different reionisation scenarios

Anne Hutter^{1,2,3*}, Maxime Trebitsch¹, Pratika Dayal¹, Stefan Gottlöber⁴, Gustavo Yepes^{5,6}, Laurent Legrand¹

¹ Kapteyn Astronomical Institute, University of Groningen, P.O. Box 800, 9700 AV Groningen, The Netherlands

² Cosmic Dawn Center (DAWN)

³ Niels Bohr Institute, University of Copenhagen, Jagtvej 128, DK-2200, Copenhagen N, Denmark

⁴ Leibniz-Institut für Astrophysik, An der Sternwarte 16, 14482 Potsdam, Germany

⁵ Departamento de Física Teórica, Modulo 8, Facultad de Ciencias, Universidad Autónoma de Madrid, 28049 Madrid, Spain

⁶ CIAFF, Facultad de Ciencias, Universidad Autónoma de Madrid, 28049 Madrid, Spain

Accepted 2023 July 18. Received 2023 July 18; in original form 2022 September 30

ABSTRACT

We use the `ASTRAEUS` framework to investigate how the visibility and spatial distribution of Lyman- α (Ly α) emitters (LAEs) during reionisation is sensitive to a halo mass-dependent fraction of ionising radiation escaping from the galactic environment (f_{esc}) and the ionisation topology. To this end, we consider the two physically plausible bracketing scenarios of f_{esc} increasing and decreasing with rising halo mass. We derive the corresponding observed Ly α luminosities of galaxies for three different analytic Ly α line profiles and associated Ly α escape fraction ($f_{\text{esc}}^{\text{Ly}\alpha}$) models: importantly, we introduce two novel analytic Ly α line profile models that describe the surrounding interstellar medium (ISM) as dusty gas clumps. They are based on parameterising results from radiative transfer simulations, with one of them relating $f_{\text{esc}}^{\text{Ly}\alpha}$ to f_{esc} by assuming the ISM of being interspersed with low-density tunnels. Our key findings are: (i) for dusty gas clumps, the Ly α line profile develops from a central to double peak dominated profile as a galaxy’s halo mass increases; (ii) LAEs are galaxies with $M_h \gtrsim 10^{10} M_\odot$ located in overdense and highly ionised regions; (iii) for this reason, the spatial distribution of LAEs is primarily sensitive to the global ionisation fraction and only weakly in second-order to the ionisation topology or a halo mass-dependent f_{esc} ; (iv) furthermore, as the observed Ly α luminosity functions reflect the Ly α emission from more massive galaxies, there is a degeneracy between the f_{esc} -dependent intrinsic Ly α luminosity and the Ly α attenuation by dust in the ISM if f_{esc} does not exceed $\sim 50\%$.

Key words: galaxies: high-redshift - intergalactic medium - dark ages, reionisation, first stars - methods: numerical

1 INTRODUCTION

The Epoch of Reionisation (EoR) marks the second major phase transition in the Universe. With the emergence of the first galaxies, ultraviolet (UV) radiation gradually ionises the neutral hydrogen (H I) in the intergalactic medium (IGM) until the Universe is reionised by $z \simeq 5.3$ (Fan et al. 2006; Keating et al. 2020; Zhu et al. 2021; Bosman et al. 2022). However, as only the brighter galaxies during the EoR are observed to date, key questions detailing the reionisation process remain outstanding: Did the few bright and more massive or the numerous faint and low-mass galaxies contribute more to reionisation? Feedback processes, such as heating by supernovae (SN) and photoionisation, suppress star formation in low-mass galaxies (Gnedin 2000; Gnedin & Kaurov 2014; Ocvirk et al. 2016, 2020; Hutter et al. 2021a), and reduce the contribution of very low-mass galaxies to reionisation. An even more critical quantity that regulates the ionising radiation (with energies $E > 13.6$ eV) escaping from galaxies and thus the galaxy population driving the reionisation of the IGM is the fraction of ionising photons f_{esc} that escape from

galaxies into the IGM (e.g. Kim et al. 2013; Seiler et al. 2019; Hutter et al. 2021b; Garaldi et al. 2022).

While the presence of H I in the IGM during the EoR impedes direct measurements of f_{esc} , different theoretical models and simulations have investigated the physical processes determining and dependencies of f_{esc} (e.g. Ferrara & Loeb 2013; Wise et al. 2014; Kimm & Cen 2014; Kimm et al. 2019). Cosmological radiation hydrodynamical simulations suggest that f_{esc} decreases towards deeper gravitational potential (e.g. Wise et al. 2014; Kimm & Cen 2014; Kimm et al. 2017, 2019; Xu et al. 2016; Anderson et al. 2017; Lewis et al. 2020). High-resolution simulations of the ISM indicate that f_{esc} is dominated by the escape from star-forming clouds. The ionising radiation of massive stars and their explosions as SN ionise, heat and destroy the star-forming clouds clearing the way for the ionising radiation to escape (Howard et al. 2018; Kim et al. 2019; He et al. 2020; Kimm et al. 2022). The complex dependency of f_{esc} on the underlying gravitational potential, the gas distribution and stellar populations in the ISM leaves marks not only in the radiation emitted by galaxies but also in the ionisation topology, the time and spatial distribution of the ionised regions around galaxies.

Current and forthcoming observations of galaxies and the ionisa-

* E-mail: anne.hutter@nbi.ku.dk

tion state of the IGM have the potential to constrain galactic properties, such as f_{esc} , and the reionisation process. On the one hand, detecting the 21 cm signal from H I in the IGM with forthcoming large radio interferometers (e.g. Square Kilometre Array) will measure the ionisation topology, which provides constraints on the dependence of f_{esc} on galaxy mass (Kim et al. 2013; Seiler et al. 2019; Hutter et al. 2020). On the other hand, being extremely sensitive to the attenuation by H I in the IGM, the observable Lyman- α ($\text{Ly}\alpha$) radiation at 1216Å from high-redshift galaxies has gained popularity in probing reionisation for the following reason: A $z \gtrsim 6$ galaxy only exhibits detectable $\text{Ly}\alpha$ emission when: (i) it is surrounded by an ionised region that is large and ionised (i.e. low residual H I fraction) enough to allow a sufficient fraction of its emerging $\text{Ly}\alpha$ line to traverse the IGM, or (ii) it is gas-rich enough (corresponding to a high H I column density) such that the red part of the $\text{Ly}\alpha$ line emerging from the galaxy is redshifted out of absorption, or (iii) it has strong outflows that redshift the emerging $\text{Ly}\alpha$ line out of absorption, or it is a combination of all three. The first criterion suggest that more massive galaxies able to retain more gas might be the most likely to show observable $\text{Ly}\alpha$ emission during the EoR: their higher rates of forming stars emitting ionising photons lead to an increased production of $\text{Ly}\alpha$ radiation in the ISM and the growth of large ionised regions around them. The latter is accelerated by their ionised regions merging earlier with those of the surrounding lower mass objects attracted by their deeper gravitational potentials (Chardin et al. 2012; Furlanetto & Oh 2016; Chen et al. 2019). As reionisation progresses and the ionised regions grow, increasingly lower mass galaxies become visible as $\text{Ly}\alpha$ emitters (LAEs), which leads not only to a higher fraction of galaxies showing $\text{Ly}\alpha$ emission but also to a reduced clustering of LAEs (McQuinn et al. 2007; Jensen et al. 2013; Hutter et al. 2015; Sobacchi & Mesinger 2015).

This picture is increasingly supported by observations of $z > 6$ LAEs. Not only the fraction of Lyman Break Galaxies (LBGs) showing $\text{Ly}\alpha$ emission rises from $z \approx 8$ to $z \approx 6$ (Schenker et al. 2014; Pentericci et al. 2014, 2018; Fuller et al. 2020), but also the majority of $\text{Ly}\alpha$ emission at $z \gtrsim 6.5$ is detected in galaxies with a bright UV continuum (Oesch et al. 2015; Zitrin et al. 2015; Roberts-Borsani et al. 2016; Endsley et al. 2022; Endsley & Stark 2022). Moreover, the close proximity of UV-bright LAEs suggests that LAEs are located in over-dense regions (Vanzella et al. 2011; Castellano et al. 2016, 2018; Jung et al. 2020; Tilvi et al. 2020; Hu et al. 2021; Endsley & Stark 2022) that exhibit the first and largest ionised regions during the EoR. This hypothesis is also in line with the observed double-peaked $\text{Ly}\alpha$ profiles in $z \gtrsim 6.5$ galaxies (Songaila et al. 2018; Hu et al. 2016; Matthee et al. 2018; Meyer et al. 2021), indicating that the ionised regions surrounding them are so large that even the part bluewards the $\text{Ly}\alpha$ resonance redshifts out of resonance. Current theoretical predictions of the large-scale LAE distribution confirm this picture, suggesting that the LAEs we see during the EoR are more massive galaxies naturally located in over-dense regions (c.f. Dayal et al. 2011; Jensen et al. 2013; Hutter et al. 2014; Mesinger et al. 2015; Weinberger et al. 2018; Qin et al. 2022).

Yet, all these LAE models effectively assume a constant f_{esc} value across the entire galaxy population at a given redshift. This assumption remains highly uncertain as f_{esc} is very sensitive to the ISM and the circumgalactic medium (CGM) of galaxies that again depend on the underlying gravitational potential of a galaxy. However, it is essential, since f_{esc} defines the critical processes that shape the $\text{Ly}\alpha$ luminosities observed from galaxies. An f_{esc} varying with galactic properties and the underlying gravitational potential might alter the galaxy population seen as LAEs for the following reasons: Firstly, within a galaxy, most $\text{Ly}\alpha$ radiation is produced by recombining hy-

drogen atoms (see e.g. Laursen et al. (2019) and Faucher-Giguère et al. (2010) for an estimate showing that $\text{Ly}\alpha$ cooling radiation is subdominant) and scales with the number of H I ionising photons absorbed within the galaxy ($\propto 1 - f_{\text{esc}}$). Secondly, a fraction of these $\text{Ly}\alpha$ photons undergoes only a few scattering events when they escape through the same low-density tunnels that facilitate the escape of H I ionising photons. In contrast, the other fraction that traverses optically thick clouds upon its escape is scattered and absorbed by hydrogen and dust, respectively (see, e.g. Verhamme et al. 2015; Dijkstra et al. 2016; Kimm et al. 2019; Kakiichi & Gronke 2021). These different escape mechanisms result not only in f_{esc} posing a lower limit to the fraction of $\text{Ly}\alpha$ photons escaping from a galaxy but also determining the $\text{Ly}\alpha$ line profile that emerges from a galaxy. Detailed low-redshift galaxy observations increasingly supported the f_{esc} -sensitivity of these $\text{Ly}\alpha$ properties (Verhamme et al. 2017; Jaskot et al. 2019; Gazagnes et al. 2020). Thirdly, f_{esc} shapes the IGM ionisation topology by determining the number of ionising photons available to ionise the IGM surrounding a galaxy. While a higher f_{esc} value enlarges the ionised region surrounding a galaxy and enhances the transmission of $\text{Ly}\alpha$ radiation through the IGM (Dayal et al. 2011; Hutter et al. 2014), the corresponding $\text{Ly}\alpha$ line emerging from a galaxy will be more peaked around the $\text{Ly}\alpha$ resonance and raise the absorption by H I in the IGM. Given this complex f_{esc} -dependency of the observed $\text{Ly}\alpha$ luminosity, it remains unclear whether different dependencies of f_{esc} with galaxy properties (e.g. increasing or decreasing with rising halo mass) would (i) identify the same galaxies as LAEs (exceeding a threshold $\text{Ly}\alpha$ luminosity) and/or (ii) lead to different spatial large-scale distribution of the LAEs' $\text{Ly}\alpha$ luminosities. In other words, which of these f_{esc} -dependent $\text{Ly}\alpha$ processes dominates the observed $\text{Ly}\alpha$ luminosities? For example, is the f_{esc} -dependency of the intrinsic $\text{Ly}\alpha$ luminosity dominant, and we yield a weaker clustering of LAEs when f_{esc} value decreases with rising halo mass? Or do they compensate each other once we reproduce the observed $\text{Ly}\alpha$ luminosity functions ($\text{Ly}\alpha$ LFs)?

To address these questions, we use our *ASTRAEUS* framework that models galaxy evolution and reionisation self-consistently (Hutter et al. 2021a; Ucci et al. 2023), and simulate different reionisation scenarios that gauge the physically plausible range of f_{esc} dependencies, i.e. f_{esc} decreasing and increasing with rising halo mass. Moreover, we parameterise results from numerical $\text{Ly}\alpha$ radiative transfer (RT) simulations of clumpy media (Gronke 2017) and build an analytic model for the fraction of $\text{Ly}\alpha$ photons escaping and the corresponding $\text{Ly}\alpha$ line profile emerging from high-redshift galaxies. Importantly, we explore three different $\text{Ly}\alpha$ line profile models, including (i) a Gaussian profile around the $\text{Ly}\alpha$ resonance where the $\text{Ly}\alpha$ escape fraction is directly related to the dust attenuation of the UV continuum (used in previous LAE models outlined in Dayal et al. 2011; Hutter et al. 2014), (ii) a $\text{Ly}\alpha$ line profile emerging from a shell of dusty gas clumps, which we model by using the different $\text{Ly}\alpha$ escape regimes identified in Gronke (2017), and (iii) a $\text{Ly}\alpha$ line profile emerging from a shell of gas clumps with a fraction f_{esc} of the solid angle interspersed by gas-free tunnels. The latter two give rise to various combinations of a central peak around the $\text{Ly}\alpha$ resonance ($\text{Ly}\alpha$ photons hardly scatter in an optically thin medium) and two peaks in the red and blue wings ($\text{Ly}\alpha$ photons are scattered in an optically thick medium). By deriving the observed $\text{Ly}\alpha$ luminosities of all simulated galaxies for all combinations of reionisation scenarios and $\text{Ly}\alpha$ line models, we address the following questions: Which f_{esc} -dependent $\text{Ly}\alpha$ process, i.e. intrinsic production, escape or transmission through the IGM of $\text{Ly}\alpha$ radiation, dominates the observed $\text{Ly}\alpha$ luminosity? Can the observed $\text{Ly}\alpha$ luminosities of galaxies inform us on their emerging $\text{Ly}\alpha$ line profile? Given the

ionisation topology depends sensitively on the assumed dependency of f_{esc} with halo mass, are the same or different galaxies identified as LAEs and do they differ in the spatial distribution of their Ly α luminosities?

This paper is organised as follows. In Section 2 we briefly describe the *ASTRAEUS* model, its implementation of dust and the different reionisation simulations. In Section 3 we introduce the different Ly α line profile models and their corresponding attenuation by dust. We then (Section 4) discuss how the Ly α line profiles depend on halo mass in our different reionisation scenarios, how free model parameters, such as the ISM clumpiness or size of the dust gas clumps, need to be adjusted to fit the observed Ly α LFs, and how the galaxy properties determining the observed Ly α luminosities depend on the halo mass of a galaxy. In Section 5 we identify the location of LAEs in the large-scale density and ionisation structure and assess whether the spatial distribution of LAEs differs for different f_{esc} -dependencies on halo mass/ionisation topologies. Finally, we briefly discuss which Lyman Break galaxies are preferentially identified as LAEs (Section 6) and conclude in Section 7. In this paper we assume a Λ CDM Universe with cosmological parameter values of $\Omega_{\Lambda} = 0.69$, $\Omega_m = 0.31$, $\Omega_b = 0.048$, $H_0 = 100h = 67.8 \text{ km s}^{-1} \text{ Mpc}^{-1}$, $n_s = 0.96$ and $\sigma_8 = 0.83$, and a Salpeter initial mass function (IMF; [Salpeter 1955](#)) between $0.1 M_{\odot}$ to $100 M_{\odot}$.

2 THE MODEL AND SIMULATIONS

In this paper, we use the *ASTRAEUS* framework. This framework couples a semi-analytic galaxy evolution model (an enhanced version of *DELPHI*; [Dayal et al. 2014](#)) with a semi-numerical reionisation scheme (*CIFOG*; [Hutter 2018](#)) and runs the resulting model on the outputs of a dark matter (DM) only N-body simulation. In this Section, we provide a brief description of the physical processes implemented in *ASTRAEUS* (for more details, see [Hutter et al. 2021a](#)) and introduce the different reionisation simulations.

2.1 N-body simulation

As part of the Multidark simulation project, the underlying DM N-body simulation (*VERY SMALL MULTIDARK PLANCK*; *VSM DPL*) has been run with the *GADGET-2 TREE+PM* code ([Springel 2005](#)). In a box with a side length of $160h^{-1} \text{ Mpc}$, it follows the trajectories of 3840^3 DM particles. Each DM particle has a mass of $6 \times 10^6 h^{-1} M_{\odot}$. For a total of 150 snapshots ranging from $z = 25$ to $z = 0$, the phase space *ROCKSTAR* halo finder ([Behroozi et al. 2013a](#)) has been used to identify all halos and subhalos down to 20 particles or a minimum halo mass of $1.24 \times 10^8 h^{-1} M_{\odot}$. To obtain the local horizontal merger trees (sorted on a redshift-by-redshift basis within a tree) for galaxies at $z = 4.5$ that *ASTRAEUS* requires as input, we have used the pipeline internal *CUTNRESORT* scheme to cut and resort the vertical merger trees (sorted on a tree-branch by tree-branch basis within a tree) generated by *CONSISTENT TREES* ([Behroozi et al. 2013b](#)). For the first 74 snapshots that range from $z = 25$ to $z = 4.5$, we have generated the DM density fields by mapping the DM particles onto 2048^3 grids and re-sampling these to 512^3 grids used as input for the *ASTRAEUS* pipeline.

2.2 Galaxy evolution

ASTRAEUS tracks key processes of early galaxy formation and reionisation by post-processing the DM merger trees extracted from the *VSM DPL* simulation. At each time step (i.e. snapshot of the N-body

simulation) and for each galaxy, it tracks the amount of gas that is accreted, the gas and stellar mass merging, star formation and associated feedback from SNII and metal enrichment, as well as the large-scale reionisation process and its associated feedback on the gas content of early galaxies.

2.2.1 Gas and stars

In the beginning, when a galaxy starts forming stars in a halo with mass M_h , it has a gas mass of $M_g^i(z) = f_g(\Omega_b/\Omega_m)M_h(z)$, with f_g being the gas fraction not evaporated by reionisation, i.e. $f_g = 1$ and $f_g < 1$ as the galaxy forms in a neutral and ionised region, respectively. In subsequent time steps a galaxy gains gas from its progenitors ($M_g^{\text{mer}}(z)$) and smooth accretion (M_g^{acc}), while its total gas mass never exceeds the limit given by reionisation feedback:

$$M_g^i(z) = \min \left(M_g^{\text{mer}}(z) + M_g^{\text{acc}}(z), f_g(\Omega_m/\Omega_b)M_h \right) \quad (1)$$

with

$$M_g^{\text{acc}}(z) = M_h(z) - \sum_{p=1}^{N_p} M_{h,p}(z + \Delta z) \quad (2)$$

$$M_g^{\text{mer}}(z) = \sum_{p=1}^{N_p} M_{h,p}(z + \Delta z), \quad (3)$$

where N_p is the galaxy's number of progenitors and $M_{h,p}$ the halo mass of each progenitor.

At each time step, a fraction of the merged and accreted (initial) gas mass is transformed into stellar mass, $M_{\star}^{\text{new}}(z) = (f_{\star}^{\text{eff}}/\Delta t)M_g^i(z)$.¹ Here f_{\star}^{eff} represents the fraction of gas that forms stars over a time span Δt and is limited by the minimum amount of stars that need to form to eject all gas from the galaxy, f_{\star}^{ej} , and an upper limit, f_{\star} . f_{\star}^{eff} depends on the gravitational potential: more massive galaxies form stars at the constant rate f_{\star} , while low-mass galaxies form stars at the limited rate f_{\star}^{ej} due to SN and radiative feedback. While we account for radiative feedback from reionisation by modifying the initial gas mass reservoir with the factor f_g , f_{\star}^{eff} incorporates the suppression of star formation in low-mass halos as gas is heated and ejected by SNII explosions. Our model incorporates a delayed SN feedback scheme, i.e. at each time step the effective star formation efficiency accounts for the SNII energy released from stars formed in the current and previous time steps, following the mass-dependent stellar lifetimes ([Padovani & Matteucci 1993](#)). In contrast to [Hutter et al. \(2021a\)](#), we have updated our model and do not assume stars to form in bursts to calculate the number of SNII exploding within a time step but $M_{\star}^{\text{new}}(z)$ to form at a constant star formation over the entire time step (see Appendix B for a detailed calculation). The star formation efficiency in the SN feedback-limited regime is given by

$$f_{\star}^{\text{ej}}(z) = \frac{v_c^2}{v_c^2 + f_w E_{51} v_z} \left[1 - \frac{f_w E_{51} \sum_j v_j M_{\star,j}^{\text{new}}(z_j)}{M_g^i(z) v_c^2} \right], \quad (4)$$

with v_c being the rotational velocity of the halo, E_{51} the energy released by a SNII, f_w the fraction of SNII energy injected into the winds driving gas outflows, $M_{\star,j}^{\text{new}}(z_j)$ the stellar mass formed during previous time steps j , and v_j the fraction of stellar mass formed in previous time step j that explodes in the current time step given the assumed IMF.

¹ We note that this definition has been altered compared to the first version of *ASTRAEUS* in ([Hutter et al. 2021a](#)).

Table 1. ASTRAEUS model parameters and chosen values in this work.

Parameter	Value or reference	Description
f_\star	0.025	Maximum star-formation efficiency
f_w	0.2	SN coupling efficiency
-	Photoionization	Radiative feedback model
IMF	Salpeter (1955)	For stellar evolution, enrichment, SED
SED	STARBURST99	ionizing SED model

ASTRAEUS incorporates multiple models for radiative feedback from reionisation, ranging from a weak and time-delayed (*Weak Heating*) to a strong instantaneous feedback (*Jeans mass*). In this work, we use the intermediate and time-delayed *Photoionisation* model, where the characteristic mass defining the gas fraction not evaporated by reionisation grows on a dynamical timescale to the respective Jeans mass (for a detailed description see [Hutter et al. 2021a](#)). We list the ASTRAEUS model parameters and their assumed values in Table 1. f_\star and f_w have been adjusted to reproduce the observed UV LFs, stellar mass functions, global star formation rate density, and global stellar mass density at $z = 10 - 5$.

2.2.2 Metals and dust

The current ASTRAEUS model also incorporates the metal enrichment by stellar winds, SNII and SNIa explosions (for a detailed description see [Ucci et al. 2023](#)). At each time step, we assume that gas smoothly accreted has the average metallicity of the gas in the IGM, Z_{IGM} . Metals are produced through stellar winds, SNII and SNIa explosions. The amount of newly forming metals depends on the number of massive stars exploding as SN in the current time step according to [Padovani & Matteucci \(1993\)](#), [Yates et al. \(2013\)](#) and [Maoz et al. \(2012\)](#). For the corresponding stellar metal yields, ASTRAEUS uses the latest yield tables from [Kobayashi et al. \(2020\)](#). We assume that gas and metals are perfectly mixed. Thus, the metals ejected from the galaxy are proportional to the ejected gas mass and the metallicity of the gas in the galaxy. This ejected metal mass contributes to Z_{IGM} .

In this work, we have extended the ASTRAEUS model ([Hutter et al. 2021a](#); [Ucci et al. 2023](#)) to follow the formation, growth, destruction, astration and destruction of dust in each galaxy (c.f. [Dayal et al. 2022](#), for details). We note that we consider dust to be part of our metal reservoir (i.e. $M_{\text{dust}} \leq M_m$). At each time step, ASTRAEUS computes the evolution of the dust mass M_{dust} in a galaxy by solving the following differential equation

$$\frac{dM_{\text{dust}}}{dt} = \dot{M}_{\text{dust}}^{\text{prod}} + \dot{M}_{\text{dust}}^{\text{grow}} - \dot{M}_{\text{dust}}^{\text{dest}} - \dot{M}_{\text{dust}}^{\text{astr}} - \dot{M}_{\text{dust}}^{\text{ej}}. \quad (5)$$

The first term on the right hand side (RHS) of Eqn. 5 denotes the production of dust in SNII and AGB stars through condensation of metals in stellar ejecta

$$\dot{M}_{\text{dust}}^{\text{prod}} = y_{\text{SNII}} \gamma_{\text{SNII}} + \dot{M}_{\text{dust}}^{\text{AGB}}, \quad (6)$$

with $y_{\text{SNII}} = 0.45 M_\odot$ being the dust mass formed per SNII,

$$\gamma_{\text{SN}}(t) = \int_{8M_\odot}^{40M_\odot} \text{SFR}(t - \tau_m) \phi(m) dm \quad (7)$$

the number of SNII events,

$$\dot{M}_{\text{dust}}^{\text{AGB}}(t) = \int_{0.85M_\odot}^{50M_\odot} y_{\text{AGB}}(m) \text{SFR}(t - \tau_m) \phi(m) dm \quad (8)$$

the contribution from AGB stars and y_{AGB} the dust yields from AGB stars. In agreement with ([Ucci et al. 2023](#)), we adopt the latest yield tables from [Kobayashi et al. \(2020\)](#) for y_{AGB} . The second term on the

RHS of Eqn. 5 describes the dust grain growth through the accretion of heavy elements in dense molecular clouds in the ISM,

$$\dot{M}_{\text{dust}}^{\text{grow}} = \left(Z' - \frac{M_{\text{dust}}}{M_g^i} \right) f_{\text{cold gas}} \frac{M_{\text{dust}}}{\tau_{\text{gg},0} Z_\odot} \quad (9)$$

where Z' is the metallicity after accretion and star formation, M_{dust} is the dust mass, $f_{\text{cold gas}}$ the fraction of cold and molecular gas, and $\tau_{\text{gg}} = \tau_{0,\text{gg}}/Z$ the accretion timescale adopted from [Asano et al. \(2013\)](#) (see also [Triani et al. 2020](#)). We assume $f_{\text{cold gas}} = 0.5$ and $\tau_{\text{gg},0} = 30 \text{ Myrs}$. The third term in Eqn. 5 describes the destruction of dust by SN blastwaves, for which we adopt the analytic description outlined in [McKee \(1989\)](#)

$$\dot{M}_{\text{dust}}^{\text{dest}} = \left(1 - f_{\text{cold gas}} \right) \frac{M_{\text{dust}}}{M_g^i} \gamma_{\text{SN}} \epsilon M_{\text{SN,bw}}, \quad (10)$$

with ϵ being the efficiency of dust destruction in a SN-shocked ISM and $M_{\text{SN,bw}}$ the mass accelerated to 100 km s^{-1} by the SN blast wave. In line with [McKee \(1989\)](#) and [Lisenfeld & Ferrara \(1998\)](#) we adopt $\epsilon = 0.03$ and $M_{\text{SN,bw}} = 6.8 \times 10^3 M_\odot$. Finally, Eqn. 5 accounts also for the destruction of dust by astration as new stars form from the metal-enriched gas,

$$\dot{M}_{\text{dust}}^{\text{astr}} = Z^i \frac{M_\star^{\text{new}}}{\Delta t}, \quad (11)$$

and the ejection of metals through winds powered by the energy injected by SN,

$$\dot{M}_{\text{dust}}^{\text{ej}} = Z' \frac{M_g^{\text{ej}}}{\Delta t}. \quad (12)$$

The parameter values (y_{SNII} , $\tau_{\text{gg},0}$, ϵ , $M_{\text{SN,bw}}$) quoted reasonably reproduce the observed UV LFs when the UV is attenuated by dust as follows (please see [Hutter et al. \(2021a\)](#) for observational UV LFs data points included): From the dust mass, M_d , we obtain the total optical depth to UV continuum photons as (see e.g. [Dayal et al. 2011](#))

$$\tau_{\text{UV,c}} = \frac{3\Sigma_d}{4as}, \quad (13)$$

with $\Sigma = M_d/(\pi r_d^2)$ being the dust surface mass density, r_d the dust distribution radius, and $a = 0.03 \mu\text{m}$ and $s = 2.25 \text{ g cm}^{-3}$ the radius and material density of graphite/carbonaceous grains ([Todini & Ferrara 2001](#)). Since we assume that dust and gas are perfectly mixed, we equate the dust distribution radius, r_d , with the radius of the gas, $r_g = 4.5\lambda r_{\text{vir}} [(1+z)/6]^{1.8}$. Here λ is the spin parameter of the simulated halo, r_{vir} the virial radius, and the third factor accounts for the redshift evolution of the compactness of galaxies and ensures that the observed UV LFs at $z = 5 - 10$ are well reproduced. For a slab-like geometry, the escape fraction of UV continuum photons of a galaxy is then given by

$$f_{\text{esc}}^c = \frac{1 - \exp(-\tau_{\text{UV,c}})}{\tau_{\text{UV,c}}}, \quad (14)$$

and its observed UV luminosity by

$$L_c^{\text{obs}} = f_{\text{esc}}^c L_c, \quad (15)$$

with the intrinsic UV luminosity, L_c , being computed as outlined in Section 2.2.4 in [Hutter et al. \(2021a\)](#).

2.3 Reionisation

At each time step ASTRAEUS follows the time and spatial evolution of the ionised regions in the IGM. For this purpose, it derives the number

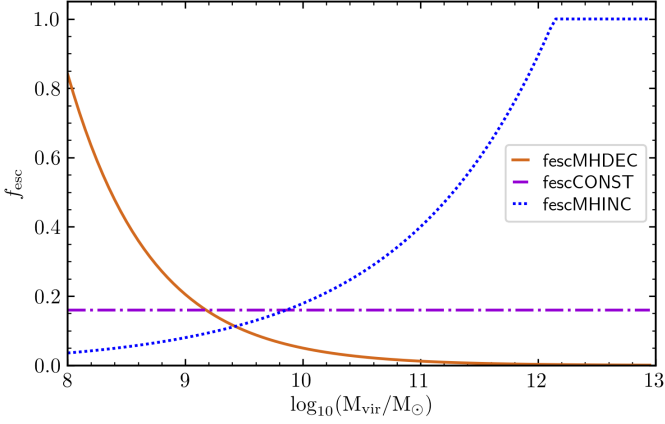


Figure 1. The ionising escape fraction f_{esc} for the three models, decreasing (solid orange line), being constant (dash dotted magenta line) and increasing (dotted blue line) with halo mass M_h .

of ionising photons produced in each galaxy, \dot{Q} , by convolving the galaxy’s star formation rate history with the spectra of a metal-poor ($Z = 0.05Z_\odot$) stellar population. Spectra have been obtained from the stellar population synthesis model `STARBUST99` (Leitherer et al. 1999). Again we assume that stars form continuously over a time step. Then the number of ionising photons that contribute to the ionisation of the IGM is then given by

$$\dot{N}_{\text{ion}} = f_{\text{esc}}\dot{Q}, \quad (16)$$

where f_{esc} is the fraction of ionising photons that escape from the galaxy into the IGM. From the resulting ionising emissivity and gas density distributions `ASTRAEUS` derives the spatial distribution of the ionised regions by comparing the cumulative number of ionising photons with the number of absorption events (see `CIFOG`, Hutter 2018, for details). Within ionised regions, it also derives the photoionisation rate and residual H I fraction in each grid cell. The ionisation and photoionisation fields obtained allow us then to determine on the fly whether the environment of a galaxy has been reionised and account for the corresponding radiative feedback by computing the gas mass the galaxy can hold on to ($f_g M_g^i$).

2.4 Simulations

In the following we consider three different reionisation scenarios that explore the physically plausible space of the ionising escape fraction f_{esc} (c.f. Fig. 1):

(i) `MHDEC`: f_{esc} decreases with rising halo mass of a galaxy (red solid line)

$$f_{\text{esc}} = f_{\text{esc,low}} \left(\frac{f_{\text{esc,high}}}{f_{\text{esc,low}}} \right)^{\frac{\log_{10}(M_h/M_{h,low})}{\log_{10}(M_{h,high}/M_{h,low})}} \quad (17)$$

with $f_{\text{esc,low}} = 0.55$, $f_{\text{esc,high}} = 0.05$, $M_{h,low} = 2 \times 10^8 h^{-1} M_\odot$ and $M_{h,high} = 10^{10} h^{-1} M_\odot$.

(ii) `MHCONST`: $f_{\text{esc}} = 0.16$ for each galaxy (magenta dash-dotted line).

(iii) `MHINC`: f_{esc} increases with rising halo mass of a galaxy (blue dotted line) following Eqn. 17 with $f_{\text{esc,low}} = 0.08$, $f_{\text{esc,high}} = 0.4$, $M_{h,low} = 10^9 h^{-1} M_\odot$ and $M_{h,high} = 10^{11} h^{-1} M_\odot$.

These three f_{esc} prescriptions have been adjusted to reproduce the

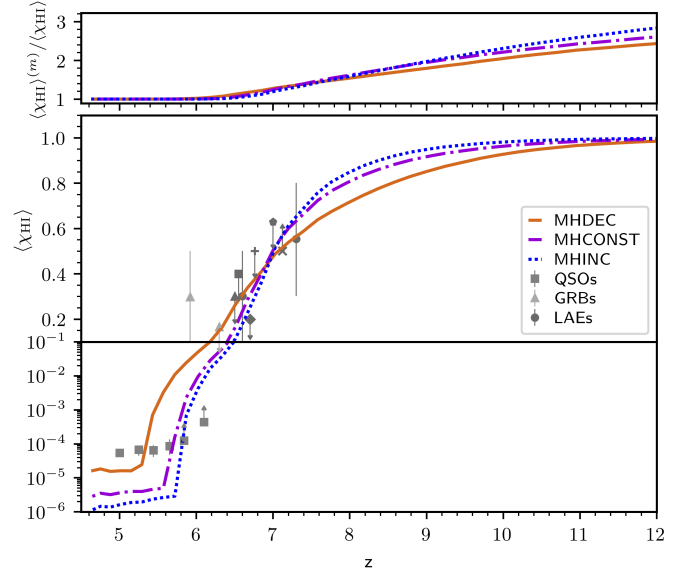


Figure 2. Ratio of the mass- and volume-averaged neutral hydrogen fraction (top panel) and volume averaged neutral hydrogen fraction (bottom panel) as a function of redshift. In each panel, we show results for our three f_{esc} models: decreasing (solid orange line), being constant (dash dotted magenta line) and increasing (dotted blue line) with halo mass M_h . In the lower panel, grey points indicate observational constraints from: GRB optical afterglow spectrum analyses (light triangles; Totani et al. 2006, 2014), quasar sightlines (Medium squares; Fan et al. 2006), Lyman- α LFs (Konno et al. 2018, dark circles), (dark squares; Kashikawa et al. 2011), (dark diamonds Ouchi et al. 2010), (dark pentagons Ota et al. 2010) and (dark triangles Malhotra & Rhoads 2004), Lyman- α emitter clustering (dark plus signs; Ouchi et al. 2010) and the Lyman- α emitting galaxy fraction (dark crosses; Pentericci et al. 2011; Schenker et al. 2012; Ono et al. 2012; Treu et al. 2012; Caruana et al. 2012, 2014; Pentericci et al. 2014).

electron optical depth measured by Planck (Planck Collaboration et al. 2020) and fit the observational constraints from LAEs, quasar absorption spectra and gamma ray bursts (as depicted in the lower panel of Fig. 2). In addition, for `MHINC` the maximum f_{esc} value of more massive galaxies is also limited by the observed Ly α LFs. Despite having very similar electron optical depths, these three f_{esc} prescriptions lead to different ionisation histories and topologies (see Fig. 2 and 6). As f_{esc} decreases with rising halo mass, reionisation is dominated by the low-mass galaxies ($M_h \lesssim 10^{10} M_\odot$), leading to on average smaller ionised regions and lower photoionisation rates. Since these low-mass galaxies appear earlier, reionisation begins earlier (see solid red line in Fig. 2); however, as shown in Hutter et al. (2021a) for the *Photoionisation* model their overall star formation rate decreases around $z \approx 7$, resulting in the Universe being reionised at a later time and exhibiting a higher average residual H I fraction in ionised regions. In contrast, as f_{esc} increases with rising halo mass, more massive galaxies ($M_h \gtrsim 10^{10} M_\odot$) drive reionisation. On average, ionised regions are larger and more clustered around more massive galaxies, and photoionisation rates within these ionised regions are higher. Reionisation begins later with the appearance of more massive galaxies and ends earlier as the abundance of these massive galaxies increases.

3 MODELLING $\text{Ly}\alpha$ EMITTERS

In this Section, we introduce the different models for the emergent $\text{Ly}\alpha$ line profiles (Section 3.1) and fractions of $\text{Ly}\alpha$ radiation escaping from a galaxy (Section 3.3), describe the attenuation of $\text{Ly}\alpha$ radiation by H I in the IGM, and the derivation of the observed $\text{Ly}\alpha$ luminosity of a galaxy (Section 3.4). We summarise the combinations of emerging $\text{Ly}\alpha$ line profile and dust attenuation models investigated in this paper in Section 3.3.3.

3.1 Emerging $\text{Ly}\alpha$ line profiles

We investigate three $\text{Ly}\alpha$ line profiles $J(x)$: (1) a thermally Doppler-broadened Gaussian centred at the $\text{Ly}\alpha$ resonance; (2) a single, double or triple-peaked profile that depends on the clumpiness and H I column density of the gas in a galaxy; (3) a single, double or triple-peaked profile that depends both on the ionising escape fraction f_{esc} and the clumpiness and H I column density of the gas in a galaxy. While the first model represents a simple assumption used in previous works (e.g. Dayal et al. 2011; Hutter et al. 2014), the latter two models are inspired by observations and detailed $\text{Ly}\alpha$ radiative transfer simulations (e.g. Dijkstra et al. 2016; Gronke 2017). The $\text{Ly}\alpha$ line emerging from a galaxy is given by the intrinsic $\text{Ly}\alpha$ luminosity, $L_{\alpha}^{\text{intr}} = \frac{2}{3}Q(1 - f_{\text{esc}})h\nu_{\alpha}$, the escape fraction $\text{Ly}\alpha$ photons from the galaxy, $f_{\text{esc}}^{\text{Ly}\alpha}$, and the line profile $J(x)$.

$$L_{\alpha}^{\text{gal}}(x) = L_{\alpha}^{\text{intr}} f_{\text{esc}}^{\text{Ly}\alpha} J(x) \quad (18)$$

Here we have expressed the frequency deviation from the $\text{Ly}\alpha$ resonance ν_{α} in terms of the thermal line broadening $\sigma_{\text{th}} = (v_{\text{th}}/c)\nu_{\alpha}$ with $v_{\text{th}} = \sqrt{2k_B T/m_{\text{H}}}$, yielding $x = \frac{\nu - \nu_{\alpha}}{\sigma_{\text{th}}}$. k_B is the Boltzmann constant, m_{H} the mass of a hydrogen atom and T the temperature of the H I gas. In the remainder of this Section, we detail our different models for the $\text{Ly}\alpha$ line profiles and escape fractions.

3.1.1 Central Gaussian

This model assumes that the emission sites of $\text{Ly}\alpha$ radiation, the hydrogen atoms within a galaxy, move at velocities that reflect the galaxy's rotation. The corresponding Doppler-broadened $\text{Ly}\alpha$ line profile is then given by

$$J_{\text{centre}}(x) = \frac{1}{\sqrt{\pi}} \frac{\sigma_{\text{th}}}{\sigma_r} \exp\left[-x^2 \frac{\sigma_{\text{th}}^2}{\sigma_r^2}\right], \quad (19)$$

We note that since the σ_{th} -dependence of x cancels any dependency of $J_{\text{Gaussian}}(\nu)$ on σ_{th} , the assumed gas temperature has no effect on the emerging $\text{Ly}\alpha$ line profile (we use $T = 10^4$ K in Fig. 3). $\sigma_r \simeq (v_r/c)\nu_{\alpha}$ describes the Doppler broadening of the line due to the rotation of the galaxy. The rotation velocity of the galaxy v_r is closely linked to the halo rotational velocity $v_c = (3\pi G H_0)^{1/3} \Omega_m^{1/6} (1+z)^{1/2} M_h^{1/3}$, ranging between $v_r = v_c$ and $v_r = 2v_c$ (Mo et al. 1998; Cole et al. 2000). We assume $v_r = 1.5v_c$.

3.1.2 Single, double or triple-peaked in a clumpy/homogeneous medium:

This model describes the $\text{Ly}\alpha$ line profile emerging from a clumpy medium. It implements the regimes and characteristic escape frequencies identified in Gronke (2017). We consider a slab with a thickness of $2B$ and a total optical depth of $2\tau_0$. The source is located at the slab's midplane and injects photons at the $\text{Ly}\alpha$ resonance

$x = 0$. If the slab medium is homogeneous, Neufeld (1990) derived the emergent $\text{Ly}\alpha$ profile as

$$J_{\text{slab}}(T, \tau_0, x) = 4\pi \frac{\sqrt{6}}{24} \frac{x^2}{a(T) \tau_0} \frac{1}{\cosh\left(\sqrt{\frac{\pi^4}{54}} \frac{|x^3|}{a(T) \tau_0}\right)}, \quad (20)$$

for $a(T)\tau_0 \gtrsim 10^3$ with $a(T) = \frac{A_{\alpha}}{4\pi\sigma_{\text{th}}(T)}$ and $\int_{-\infty}^{\infty} J_{\text{slab}}(x, x_i) dx = 1$. A_{α} is the Einstein for the spontaneous emission of $\text{Ly}\alpha$ photons.

In the following we will revisit the regimes for $\text{Ly}\alpha$ escape in a clumpy medium that have been identified in Gronke (2017). The clumpy medium is characterised by the total optical depth of the clumps and the average number of clumps each $\text{Ly}\alpha$ photon escaping the slab scatters with. For a slab consisting of clumps with each having an optical depth $\tau_{0,\text{cl}}$ at the line centre, $\text{Ly}\alpha$ photons escaping the slab will encounter on average f_c clumps and have a total optical depth of $\tau_0 = \frac{4}{3}f_c\tau_{0,\text{cl}}$ ² at the line centre. The emerging $\text{Ly}\alpha$ line profile depends sensitively on the total and clump optical depth at line centre, τ_0 and $\tau_{0,\text{cl}}$, respectively, and the number of clumps the $\text{Ly}\alpha$ photons scatter with. Gronke (2017) identified the following regimes:

- *Free-streaming regime:* The clumpy medium is optically thin ($\tau_0 < 1$), and $\text{Ly}\alpha$ photons can stream through. The emerging line profile peaks around $x = 0$.

- *Porous regime:* The clumps are optically thick to $\text{Ly}\alpha$ photons ($\tau_{\text{cl}} > 1$), but only a fraction $1 - \exp(-\tau_{0,\text{cl}})$ of the $\text{Ly}\alpha$ photons scatter with a clump. The emerging line profile is again peaked around $x = 0$.

- *Random walk regime:* The clumps are optically thick to $\text{Ly}\alpha$ ($\tau_{\text{cl}} > 1$), and each $\text{Ly}\alpha$ photon encounters $N_{\text{sct},\text{rw}} \propto f_c^2$ scattering events (Hansen & Oh 2006). However, the number of scattering events is too low for the $\text{Ly}\alpha$ photons to scatter in frequency space far enough into the wings to escape through excursion. Hence, the emerging line profile peaks also around $x = 0$.

- *Homogeneous regime:* The clumps are optically thin ($\tau_{\text{cl}} \leq 1$) and $\text{Ly}\alpha$ photons scatter $\sim \tau_0$ times ($N_{\text{sct},\text{exc}} \propto f_c$) and escape via excursion: they follow a random walk in space *and* frequency and escape as they are scattered into the wings where the clumps become optically thin. The emerging line profile is a double-peaked with the two peaks being located at

$$x_{\text{esc}}(\tau_0) \simeq \begin{cases} \pm (ka\tau_0/\sqrt{\pi})^{1/3}, & \frac{\sqrt{\pi}x_{\star}^2}{ka} \leq \tau_0 \\ \pm x_{\star}, & \tau_0 < \frac{\sqrt{\pi}x_{\star}^2}{ka} \end{cases} \quad (21)$$

for an injection frequency $x = 0$ (c.f. Adams 1975; Gronke 2017). Here x_{\star} is the frequency where the $\text{Ly}\alpha$ absorption profile transitions from the Gaussian core to the Lorentzian wings, and $\tau_0 = \frac{\sqrt{\pi}x_{\star}^2}{ka}$ marks the transition where the slab becomes optically thin at the escape frequency x_{esc} .

Gronke (2017) derived the boundary criteria between these regimes for a static clumpy medium, which we briefly revisit here. To derive the critical number of clumps, f_c , separating the regimes, we first consider the time and distances covered that it takes a $\text{Ly}\alpha$ to traverse the slab.

Excursion: As $\text{Ly}\alpha$ photons traverse or escape the slab, they scatter with H I many times. This alters their direction and frequency x , and they essentially perform a random walk. However, as the $\text{Ly}\alpha$ cross section is higher close to the line centre, most scatterings will occur close to the line centre and remain spatially close.

² The factor 4/3 arises from the mean path length through a sphere.

Only as the Ly α photons are scattered into the wings of the Ly α absorption profile their mean free paths become larger, allowing them to escape the slab (Adams 1975). The series of these so-called wing scatterings that allow Ly α photons to escape are referred to as excursion. We can estimate the mean displacement and time spent in such an excursion event: a Ly α photon with frequency x will scatter on average $N_{\text{sct,exc}} \sim x^2$ times before it returns to the core. For a slab of thickness B , its average mean free path is $\lambda_{\text{mfp,exc}}(x) = B\sigma_0/(k\tau_0\sigma_{\text{HI}}(x)) = B/(k\tau_0H(a, x))$ using the wing approximation of the Ly α cross section and $k \simeq \sqrt{3}$ being a geometrical factor that accounts for slant paths in a plane-parallel medium and was determined in Adams (1975).³ This and the random walk nature of the Ly α escape imply an average displacement of

$$d_{\text{exc}} = \sqrt{N_{\text{sct,exc}}}\lambda_{\text{mfp,exc}}(x) = \frac{\sqrt{N_{\text{sct,exc}}}B}{k\tau_0H_v(a, x)} = \frac{xB}{k\tau_0H_v(a, x)} \quad (22)$$

and time spent in the excursion of

$$t_{\text{exc}} = N_{\text{sct,exc}} \frac{\lambda_{\text{mfp,exc}}(x)}{c} = \frac{N_{\text{sct,exc}}B}{ck\tau_0H_v(a, x)} = \frac{x^2B}{ck\tau_0H_v(a, x)}, \quad (23)$$

with $H_v(a, x) = \frac{a}{\sqrt{\pi}(x)^2}$ being the effective line absorption profile in the wings.

Random Walk: As the clumps become optically thick at corresponding escape frequencies $x_{\text{esc}}(\tau_0)$, the Ly α photons do not escape the slab via excursion anymore but by random walking: the number of scattering events is smaller than required for excursion and scale with the square of the number of clumps, $N_{\text{sct,rw}} \propto f_c^2$ (Hansen & Oh 2006). With the mean free path given by the average clump separation $\lambda_{\text{mfp,rw}} = kB/f_c$, the average displacement and time are then

$$d_{\text{rw}} = \sqrt{N_{\text{sct,rw}}}\lambda_{\text{mfp,rw}} = \frac{\sqrt{N_{\text{sct,rw}}}kB}{f_c} = kB \quad (24)$$

and

$$t_{\text{rw}} = \sqrt{N_{\text{sct,rw}}} \frac{\lambda_{\text{mfp,rw}}}{c} = \frac{\sqrt{N_{\text{sct,rw}}}kB}{cf_c} = \frac{kBf_c}{c}. \quad (25)$$

(i) *Division between random-walk and homogeneous regime in optically thick medium:* For a given total optical depth at the line centre, τ_0 , we can derive the critical number of clumps along a line of sight that marks the transition from the random (clumps are optically thick) to the homogeneous regime (clumps become optically thick at the excursion frequency). We estimate this transition to arise when both regimes contribute equally to the flux of escaping Ly α photons.

$$\frac{F_{\text{rw}}}{F_{\text{exc}}} = \frac{t_{\text{exc}}}{t_{\text{rw}}} = \frac{x^2}{k^2\tau_0H(x)f_c} = \frac{\sqrt{\pi}x^4}{k^2a\tau_0f_c} = 1 \quad (26)$$

With $\tau_0 = 4/3f_c\tau_{0,\text{cl}}$, the critical number of clumps for Ly α photons escaping at frequency x yields then as

$$f_{c,\text{crit}} = \frac{\sqrt{3}\pi^{1/4}}{2k} \frac{x^2}{\sqrt{a\tau_{0,\text{cl}}}}. \quad (27)$$

As long as the wings remain optically thick, the majority of Ly α photons (with injection frequency $x = 0$) will escape at $x_{\text{esc}} \simeq \left(\frac{ka\tau_0}{\sqrt{\pi}}\right)^{1/3}$

leading to

$$f_{c,\text{crit}} = \frac{2}{\sqrt{3}k\pi^{1/4}} \sqrt{a\tau_{0,\text{cl}}} \quad (28)$$

This $f_{c,\text{crit}}$ value marks the transition from the random walk to the excursion regime. We can understand its increase with the clump optical depth $\tau_{0,\text{cl}}$ as follows: for optically thicker clumps to become optically thin at the escape frequency x_{esc} , a higher escaping frequency and thus a higher effective total optical depth are required. This can only be achieved by interacting with more clumps (higher $f_{c,\text{crit}}$).

Because the transition described by $f_{c,\text{crit}}$ is not sharp, we model the Ly α line profile emerging from the moving slab by superposing the Ly α radiation escaping in the homogeneous (J_{slab}) and random walk regimes (J_{centre}).

$$J_{\text{rh}}(\tau_0, x) = (1 - f_{\text{rw}})J_{\text{slab}}(T, \tau_0, x) + f_{\text{rw}}J_{\text{centre}}(T, x) \quad (29)$$

Here we assume J_{centre} is given by Eqn. 19 with $\sigma_r = \sigma_{\text{th}}$ and

$$J_{\text{slab}}(T, \tau_0, x) = \begin{cases} 4\pi \frac{\sqrt{6}}{24} \frac{x^2}{a(T)\tau_0} \frac{1}{\cosh\left(\sqrt{\frac{\pi^4}{54}} \frac{|x^3|}{a(T)\tau_0}\right)}, & \frac{\sqrt{\pi}x^2}{ka(T)} \leq \tau_0 \\ 4\pi \frac{\sqrt{6}}{24} \frac{kx^2}{\sqrt{\pi}x_\star^3} \frac{1}{\cosh\left(\sqrt{\frac{\pi^3}{54}} \frac{k|x^3|}{x_\star^3}\right)}, & \tau_0 < \frac{\sqrt{\pi}x^2}{ka(T)}. \end{cases} \quad (30)$$

We derive the corresponding ratio f_{rw} by assuming that the Ly α flux escapes predominantly where the Ly α profiles peak,

$$f_{\text{rw}} = \frac{F_{\text{rw}}/F_{\text{exc}}}{F_{\text{rw}}/F_{\text{exc}} + \frac{J_{\text{centre}}(0)}{2(J_{\text{slab}}(\tau_0, x_{\text{esc}}) + J_{\text{slab}}(\tau_0, -x_{\text{esc}}))}}. \quad (31)$$

We note that J_{slab} reproduces the results of Ly α radiative transfer simulations down to $\tau_0 \simeq 10^5$. While the line profiles for lower τ_0 values start deviating, we will see in Section 3.2 that the galaxies considered here exceed this threshold. Importantly, we find that the assumed J_{slab} , J_{centre} and f_{rw} reproduce the Ly α line profiles for resting clumps, fixed τ values, and varying f_c values in Gronke (2017).

(ii) *Division between porous and homogeneous regime in optically thin medium:* As the medium becomes optically thinner, Ly α photons that scatter into the wings can escape the slab before completing their excursion. This transition occurs as the wings become optically thin, i.e. $k\tau(x_\star) \leq 1$ translating to $ka\tau_0 \leq \sqrt{\pi}x_\star^2$, and Ly α photons escape at $x_{\text{esc}} = x_\star$. While the slab is optically thin at x_\star , depending on whether the clumps are optically thin or thick at x_{esc} , the escape of Ly α photons is described by the homogeneous and porous regime, respectively. Again we estimate the transition to arise when both regimes contribute equally to the flux of escaping Ly α photons.

$$\frac{F_{\text{por}}}{F_{\text{hom}}} = \frac{t_{\text{exc}}}{t_{\text{rw}}} = \frac{\sqrt{\pi}x_\star^4}{k^2a\tau_0f_c} = 1 \quad (32)$$

We yield the critical number of clumps that mark the transition from the porous to the homogeneous regime as

$$f_{c,\text{crit}} = \frac{x_\star}{k(1 - e^{-\tau_{0,\text{cl}}})}. \quad (33)$$

We note that if clumps are optically thin at line centre ($\tau_{0,\text{cl}} < 1$), not every clump encounter leads to a scattering event; this reduces the number of clumps encountered by a factor $1 - e^{-\tau_{0,\text{cl}}}$. The emerging Ly α line profile accounts again for Ly α photons escaping in homogeneous (J_{slab} , see Eqn. 30) and porous regime (J_{centre} , see Eqn.

³ The geometrical factor k is often not explicitly included in the literature when displacements and excursion times are discussed.

19).

$$J_{\text{ph}}(\tau_0, x) = (1 - f_{\text{por}})J_{\text{slab}}(T, \tau_0, x) + f_{\text{por}}J_{\text{centre}}(T, x) \quad (34)$$

The ratio between the two different escape regimes is then again given by assuming that most Ly α photons escape at the peak frequencies,

$$f_{\text{por}} = \frac{F_{\text{por}}/F_{\text{hom}}}{F_{\text{por}}/F_{\text{hom}} + \frac{J_{\text{centre}}(0)}{2(J_{\text{slab}}(\tau_0, x_{\text{esc}}) + J_{\text{slab}}(\tau_0, -x_{\text{esc}}))}}. \quad (35)$$

(iii) *Division between porous and random-walk regime:*

As the optical depth of the already optically thick clumps, $\tau_{0,\text{cl}}$, exceeds the optical depth of the slab, τ_0 , a fraction of the Ly α photons traverse the slab without scattering, leaving the random and entering the porous regime. This transition occurs as the number of clumps encountered by the Ly α photons becomes less than unity, $f_c < 1$.

3.1.3 Ionising escape fraction dependent in a clumpy/homogeneous medium

For this Ly α line profile model, we assume a model similar to the so-called picket fence model (Heckman et al. 2011). Here a fraction f_{esc} of the ionising radiation escapes through low-density channels, while the other fraction of ionising photons is absorbed by the dense shell. Correspondingly, the Ly α photons escaping through the channels scatter only a few times, while those escaping through the shell encounter many scattering events. For optically thin channels, the former gives rise to a single-peaked Ly α line centred around $x = 0$, while the latter creates a broader double-peaked Ly α line (assuming a homogeneous slab model with peaks at x_{esc}).

Here we assume the channels to be fully ionised and a fraction f_{esc} of the Ly α photons to escape through them without scattering. As a consequence, the other fraction of Ly α photons encounter the shell with an optical depth of

$$\tau_{\text{shell}} = \frac{\tau_0}{1 - f_{\text{esc}}}, \quad (36)$$

at their first scattering. τ_0 is the optical depth as derived in Section 3.2. We make the simplifying assumption that those photons traverse the shell without being scattered into the channels. In reality a fraction of these photons encounter a lower optical depth when traversing the empty channels on their scattering path out of the slab, leading to a profile closer centered around $x = 0$. Thus, the emerging Ly α line profile, which we assume to be

$$J(\tau, x) = f_{\text{esc}} J_{\text{slab}}(T, 0, x) \quad (37)$$

$$+ (1 - f_{\text{esc}}) J_{\text{shell}}(T, \tau_{\text{shell}}, x)$$

$$J_{\text{shell}} = f_{\text{shell}} J_{\text{slab}}(T, 0, x) \quad (38)$$

$$+ (1 - f_{\text{shell}}) J_{\text{slab}}(T, \tau_{\text{shell}}, x)$$

represents a lower limit to the fraction of Ly α photons escaping close to the resonance. We derive f_{shell} by choosing a clump optical depth $\tau_{0,\text{cl}}$ and use Eqn 31 and 35 for the random-homogeneous ($k\alpha\tau_0 > \sqrt{\pi}x_{\star}^3$) or porous-homogeneous ($k\alpha\tau_0 < \sqrt{\pi}x_{\star}^3$) transitions.

3.2 Optical depth and H I column density

To derive the Ly α line profile emerging from a simulated galaxy for the models described in Sections 3.1.2 (*Clumpy* model) and 3.1.3

(*Porous* model), we yield the optical depth at the Ly α line centre from our simulated galaxies as

$$\tau_0 = \frac{4}{3} f_c \tau_{0,\text{cl}} = N_{\text{HI}} \sigma_{\text{HI}}. \quad (39)$$

$\tau_{0,\text{cl}}$ is a free parameter in our model and reflects the optical depth of a dense clump in the ISM. We will use this parameter to calibrate our model to the observed Ly α LFs at $z = 6.6 - 8$ in Section 4. To obtain a rough estimate of $\tau_{0,\text{cl}}$, we consider the median mass (M_{cl}) and size (r_{cl}) of molecular clouds ($M_{\text{cl}} \approx 10^5 M_{\odot}$ and $r_{\text{cl}} = 20$ pc) resembling the mass and size of possible dense structures in the ISM,

$$\tau_{0,\text{cl}} = \sigma_{\text{HI}} \frac{M_{\text{cl}}}{r_{\text{cl}}}. \quad (40)$$

To obtain the optical depth τ_0 , we derive the neutral hydrogen column density N_{HI} from the initial gas mass, M_{g}^i as

$$\begin{aligned} N_{\text{HI}} &= \xi \frac{3M_{\text{HI}}}{4\pi r_g^2 m_{\text{H}}} = \xi \frac{3X_c(1-Y)M_{\text{g}}^i}{4\pi(4.5\lambda r_{\text{vir}})^2 m_{\text{H}}} = \xi \frac{3f_m M_{\text{vir}}}{81\pi\lambda^2 r_{\text{vir}}^2 m_{\text{H}}} \\ &= \xi \left(\frac{9\pi^2 H_0^2 \Omega_m}{G} \right)^{2/3} (1+z)^2 M_{\text{vir}}^{1/3} \frac{3f_m}{81\pi\lambda^2 m_{\text{H}}}. \end{aligned} \quad (41)$$

Here r_g describes the gas radius, for which we assume $r_g = 4.5\lambda r_{\text{vir}}$. X_c and Y are the cold gas and helium mass fractions, respectively. Gas accretion and SN feedback processes determine the relation between the initial gas mass and the halo mass, f_m , which ranges typically between $\sim 10^{-3}$ for low-mass galaxies to $\sim 10^{-1}$ for more massive galaxies. ξ is a geometrical correction factor that depends on τ_0 and the dust optical depth at the Ly α resonance τ_d . Its maximum values is 0.35 and we describe its derivation and dependencies in Appendix A. For the cosmological parameters assumed in this paper, we yield

$$N_{\text{HI}} = 6.5 \times 10^{17} \text{ cm}^2 (1+z)^2 \frac{\xi f_m}{\lambda^2} \left(\frac{M_{\text{vir}}}{10^8 M_{\odot}} \right)^{1/3}. \quad (42)$$

3.3 Dust attenuation

We employ two different dust models. The first one links the Ly α escape fraction to the escape fraction of UV continuum photons, f_{esc}^c . The second one is more complex. It assumes a clumpy medium where the attenuation of Ly α by dust follows different relations in the regimes identified in Gronke (2017). Both models assume a slab-like geometry and we describe their details in the following.

3.3.1 Simple attenuation model

In this model, we assume that (i) dust and gas are perfectly mixed, (ii) the dust distribution is slab-like, and (iii) the dust attenuation of Ly α photons is proportional to the dust attenuation of UV continuum photons. The escape fraction of Ly α photons, $f_{\text{esc}}^{\text{Ly}\alpha}$, is then directly related to the escape of UV continuum photons, f_{esc}^c , derived in Section 2.2.2.

$$f_{\text{esc}}^{\text{Ly}\alpha} = p f_{\text{esc}}^c \quad (43)$$

We use p as a free parameter to obtain the observed Ly α luminosity functions at $z = 6.6 - 7.3$.

3.3.2 Refined attenuation model

This model assumes that dust and gas are perfectly mixed and distributed in clumps. The dust attenuation of Ly α photons depends on

the total optical depth of the dust, $\tau_{d,\text{total}}$, the optical depth of a clump, $\tau_{d,\text{cl}}$, and the number of clumps, f_c , encountered along the sightline from the midplane to the surface of the slab. We derive its value by estimating the dust absorption cross section. Following Galliano (2022) and assuming the radius and density of graphite/carbonaceous grains (see Section 2.2.2), we assume $\kappa_{\text{abs}} \simeq \frac{Q_{\text{abs}}}{a^2} \simeq 2 \times 10^5 \text{ cm}^2/\text{g}$ with $Q_{\text{abs}} \simeq 1$ being the absorption efficiency.⁴

$$\tau_{d,\text{total}} = \frac{4}{3} f_c \tau_{d,\text{cl}} = \xi \frac{3}{4\pi} \frac{M_d}{r_d^2} \kappa = \frac{M_d}{M_{\text{HI}}} \frac{\kappa_{\text{abs}} m_{\text{H}}}{\sigma_{\text{HI}}} \tau_0 \quad (44)$$

The resulting estimates for $\tau_{d,\text{total}}$ and $\tau_{d,\text{cl}}$ allow us to compute the Ly α escape fractions in the different escape regimes as follows.

3.3.2.1 Free-streaming regime: In an optically thin slab ($\tau_0 < 1$), the Ly α photons stream through $\sim f_c$ clumps. On their way, they are attenuated by the dust in clumps and hence, the total dust optical depth determines the Ly α escape fraction, $\tau_{d,\text{total}}$, as

$$f_{\text{esc}}^{\text{Ly}\alpha,\text{fs}} = \exp(-\tau_{d,\text{total}}) = \exp\left(-\frac{4}{3} f_c \tau_{d,\text{cl}}\right) \quad (45)$$

We note that in this regime, the number of clumps along the sightline f_c and clump optical depth $\tau_{0,\text{cl}}$ are degenerate.

3.3.2.2 Random walk regime: In the random walk regime, both the slab and individual clumps are optically thick ($\tau_{\text{cl}} \geq 1$). As a result, Ly α photons escape by mostly being scattered by the clumps, and their escape fraction is determined by the number of clumps encountered along their random walk, $N_{\text{cl}}(f_c)$, and the absorption probability per clump interaction ϵ . According to Hansen & Oh (2006), it is then given by

$$f_{\text{esc}}^{\text{Ly}\alpha,\text{rw}} = f_{\text{HO06}} = \frac{1}{\cosh(\sqrt{2N_{\text{cl}}(f_c)} \epsilon)} \quad (46)$$

We assume $N_{\text{cl}}(f_c) \simeq \frac{3}{2} f_c^2 + 2f_c$ as found in Gronke (2017). The scaling of N_{cl} with f_c also agrees with the findings in Hansen & Oh (2006) and prefactors vary slightly due to different geometries of the scattering surface. However, since ϵ is sensitive to how deep the photons permeate the clump, it depends non-trivially on the clump optical depth and movement. For simplicity, we assume $\epsilon = 1 - \exp(-\tau_{d,\text{cl}}^{2/3}/10)$, which we have found to be in rough agreement with the fits and results shown in Gronke (2017).

3.3.2.3 Homogeneous regime: In the homogeneous regime, the slab is optically thick ($\tau_0 \geq 1$), while the individual clumps are optically thin at the escape frequencies ($\tau_{\text{cl}}(x_{\text{esc}}) < 0$). During their initial random walk, the Ly α photons scatter with $N_{\text{cl}}(f_{c,\text{crit}})$ clumps before they diffuse into the wings and escape by free-stream through f_c clumps. The resulting Ly α escape fraction,

$$f_{\text{esc}}^{\text{Ly}\alpha,\text{hom}} = f_{\text{HO06}}(f_{c,\text{crit}}) \exp(-\tau_{d,\text{total}}), \quad (47)$$

⁴ We note that this is in rough agreement with the dust extinction cross sections of the Small and Large Magellanic clouds $\kappa_{\text{ext}} = \sigma_d/m_{\text{H}} = \sigma_{d,\text{ref}} \frac{M_z}{Z_{\text{ref}} m_{\text{H}}} \simeq 4 \times 10^5 \text{ cm}^2/\text{g}$, with the extinction efficiency $Q_{\text{ext}} = Q_{\text{abs}} + Q_{\text{sca}}$ being given by the similar sized absorption (Q_{abs}) and scattering efficiencies (Q_{sca}) at Ly α , a dust-to-metal mass ratio $M_d/M_z \simeq 0.25$, $\sigma_{\text{ref}} \simeq 4 \times 10^{-22} \text{ cm}^2$ and $Z_{\text{ref}} \simeq 0.0025$ for SMC and $\sigma_{\text{ref}} \simeq 7 \times 10^{-22} \text{ cm}^2$ and $Z_{\text{ref}} \simeq 0.005$ for LMC (for further explanations see Laursen 2010).

depends on $f_{c,\text{crit}}$ and $\tau_{d,\text{total}}$, with $f_{c,\text{crit}}$ being determined by τ_0 and $\tau_{0,\text{cl}}$.

$$f_{c,\text{crit}} = \begin{cases} \frac{2}{\sqrt{3} k \pi^{1/4}} \sqrt{a \tau_{0,\text{cl}}} & \text{for } k a \tau_0 \geq \sqrt{\pi} x_{\text{max}}^2 \\ \frac{x_{\text{max}}}{k(1 - e^{-\tau_{0,\text{cl}}})} & \text{for } k a \tau_0 < \sqrt{\pi} x_{\text{max}}^2 \end{cases} \quad (48)$$

3.3.2.4 Porous regime: In the porous regime, the individual clumps are optically thick ($\tau_{0,\text{cl}} \geq 1$), but only a fraction $1 - e^{-f_c}$ of the Ly α photons will encounter a clump along their sightlines. The other fraction of Ly α photons does not interact with any clumps and is thus not attenuated by dust as they escape the slab.⁵

$$f_{\text{esc}}^{\text{Ly}\alpha,\text{por}} = e^{-f_c} + \left[1 - e^{-f_c}\right] \exp\left(-\frac{4}{3} f_c \tau_{d,\text{cl}}\right) \quad (49)$$

3.3.3 Emerging Ly α line profile models

We briefly summarize the combinations of Ly α line and dust attenuation models that we will investigate in this paper.

Gaussian: The Ly α line profile emerging from a galaxy is given by the central Gaussian Ly α line profile (Section 3.1.1). To account for the attenuation by dust, we apply the Ly α escape fraction, $f_{\text{esc}}^{\text{Ly}\alpha}$, derived in our simple dust model (Section 3.3.1) to all frequencies x .

Clumpy: This model assumes a shell of dusty gas clumps, whereas gas and dust are perfectly mixed. It combines the Ly α line model described in Section 3.1.2 with the refined dust model depicted in Section 3.3.2. The gas in the galaxies is assumed to have a temperature of $T = 10^4 \text{ K}$.⁶ In contrast to the *Gaussian* model, we dust-attenuate the Ly α line of each escape regime (homogeneous, random, porous) by its corresponding escape fraction $f_{\text{esc}}^{\text{Ly}\alpha}$. The emerging Ly α line profile is then the superposition of the line profiles of all relevant escape regimes,

$$L_{\alpha}^{\text{gal}}(x) = f_{\text{esc},\text{slab}}^{\text{Ly}\alpha} (1 - f) J_{\text{slab}}(x) + f_{\text{esc},\text{centre}}^{\text{Ly}\alpha} f J_{\text{centre}}(x), \quad (50)$$

with $f_{\text{esc},\text{slab}}^{\text{Ly}\alpha} = f_{\text{esc},\text{hom}}^{\text{Ly}\alpha}$ and $(f, f_{\text{esc},\text{centre}}^{\text{Ly}\alpha})$ given by $(1, f_{\text{esc},\text{fs}}^{\text{Ly}\alpha})$, $(f_{\text{rw}}, f_{\text{esc},\text{rw}}^{\text{Ly}\alpha})$ or $(f_{\text{por}}, f_{\text{esc},\text{por}}^{\text{Ly}\alpha})$ depending on the total and clump optical depths τ_0 and $\tau_{0,\text{cl}}$.

Porous: This model is very similar to the *Clumpy* model. However, it considers the shell of clumps to be pierced with gas and dust-free channels through which a fraction f_{esc} of the Ly α photons escape without scattering. It combines the Ly α line model described in Section 3.1.3 and assuming $\tau_{\text{channel}}^{\text{Ly}\alpha} = 0$ with the refined dust model depicted in Section 3.3.2. Again we assume the gas in the galaxy to be heated to a temperature of $T = 10^4 \text{ K}$, and the Ly α line of each escape regime (homogeneous, random, porous) to be dust-attenuated by its corresponding escape fraction $f_{\text{esc}}^{\text{Ly}\alpha}$. The emerging Ly α line

⁵ We note that our expression is here a lower limit of $f_{\text{esc}}^{\text{Ly}\alpha,\text{por}}$ as we assume the Ly α radiation interacting with clumps to experience attenuation as if they streamed through the clump. It might be more appropriate to consider these Ly α photons to be absorbed as in the random walk regime, $f_{\text{esc}}^{\text{Ly}\alpha,\text{por}} = e^{-f_c} + \left[1 - e^{-f_c}\right] \frac{1}{\cosh(\sqrt{2N_{\text{cl}}(f_c)} \epsilon)}$, however in practise galaxies in the porous regime have not much, if any, dust.

⁶ We have chosen $T = 10^4 \text{ K}$ for simplicity. If we were to assume the virial temperature (T_{vir}), the double-peak line profile would narrow as T_{vir} increases.

profile is again a superposition of the Ly α photons escaping through the channels and the clumpy shell,

$$L_{\alpha}^{\text{gal}}(x) = f_{\text{esc}} J_{\text{channel}}(x) + (1 - f_{\text{esc}}) J_{\text{shell}}(x) \quad (51)$$

$$J_{\text{channel}}(x) = J_{\text{centre}}(x) \quad (52)$$

$$J_{\text{shell}}(x) = f_{\text{esc,slab}}^{\text{Ly}\alpha} (1 - f) J_{\text{slab}}(x) + f_{\text{esc,centre}}^{\text{Ly}\alpha} f J_{\text{centre}}(x) \quad (53)$$

with $f_{\text{esc,slab}}^{\text{Ly}\alpha} = f_{\text{esc,hom}}^{\text{Ly}\alpha}$, and $(f, f_{\text{esc,centre}}^{\text{Ly}\alpha})$ given by $(1, f_{\text{esc,fs}}^{\text{Ly}\alpha})$, $(f_{\text{rw}}, f_{\text{esc,rw}}^{\text{Ly}\alpha})$ or $(f_{\text{por}}, f_{\text{esc,por}}^{\text{Ly}\alpha})$ depending on the total and clump optical depths τ_0 and $\tau_{0,\text{cl}}$. We note that τ_0 exceeds the τ_0 value in the *Clumpy* model when $f_{\text{esc}} > 0$ (see Eqn. 36), as the same amount of gas and dust is distributed over a smaller solid angle.

3.4 IGM attenuation

The Ly α radiation escaping from a galaxy is attenuated by the H I it encounters along the line of sight from the location of emission, $r(z_{\text{em}})$, to the location of absorption, $r(z_{\text{obs}})$. Expressing the frequency ν of a photon in terms of its rest-frame velocity $x = v/b = (\nu_{\alpha}/\nu - 1)c/b$ relative to the Ly α line centre, the transmitted fraction of radiation at frequency x is given by

$$T_{\alpha,x}(x) = \exp[-\tau_{\alpha}(x)] \quad (54)$$

$$\tau_{\alpha}(x) = c \int_{z_{\text{em}}}^{z_{\text{obs}}} \sigma_0 \phi(x + x_p(r(z))) \frac{n_{\text{HI}}(r(z))}{(1+z)H(z)} dz. \quad (55)$$

Here τ_{α} describes the optical depth to Ly α , while $n_{\text{HI}}(r)$ and $v_p(r) = bx_p(r)$ the H I density and peculiar velocity (in the rest-frame of the emitted Ly α radiation) at a physical distance r from the emitter, respectively. σ_0 is the specific absorption cross section, described in the cgs system as

$$\sigma_0 = \frac{\pi e^2 f}{m_e c^2} = \frac{3\lambda_{\alpha}^2 A_{21}}{8\pi}, \quad (56)$$

where $f = 0.4162$ is the oscillator strength, e the electron charge, m_e the electron mass, $\lambda_{\alpha} = 1216\text{\AA}$ the wavelength of a photon at the Ly α line centre, and $A_{21} = 6.265 \times 10^8 \text{s}^{-1}$ the Einstein coefficient for spontaneous emission of Ly α photons. $\phi(x)$ depicts the Ly α profile for absorption and is given by a Voigt profile consisting of a Gaussian core

$$\phi_{\text{Gauss}}(x) = \frac{\lambda_{\alpha}}{\sqrt{\pi}b} \exp(-x^2) \quad (57)$$

$$b = \sqrt{\frac{2k_B T_{\text{IGM}}}{m_H}}, \quad (58)$$

and Lorentzian damping wings

$$\phi_{\text{Lorentz}}(x) = \frac{A_{21}\lambda_{\alpha}^2}{4\pi^2(xb)^2 + \frac{1}{4}A_{21}^2\lambda_{\alpha}^2}. \quad (59)$$

Here b is the Doppler parameter, T_{IGM} the temperature of the IGM, k_B the Boltzmann constant, and m_H the mass of a hydrogen atom. While pressure line broadening is unimportant in regions of low H I density and the profile can be approximated by the Gaussian core, the absorption in the Lorentzian damping wings is non-negligible in regions of high H I density. In practise, we mimic the Voigt profile by assuming the Gaussian core profile $\phi(x) = \phi_{\text{Gauss}}(x)$ for $|x| < x_{\star}$ and the Lorentzian wing profile $\phi(x) = \phi_{\text{Lorentz}}(x)$ otherwise. Fitting to numerical results yields the transition frequency as

$$x_{\star} = 0.54 \log_{10} \left(\frac{b}{\text{cm/s}} \right) \quad (60)$$

Parameter	Scenario	Gaussian	Clumpy	Porous
$\tau_{0,\text{cl}}$	MHDEC	-	1.2×10^6	2.4×10^6
$\tau_{0,\text{cl}}$	MHINC	-	5×10^5	1.8×10^6
p	MHDEC	1.0	-	-
p	MHINC	1.4	-	-
T	all	10^4 K	10^4 K	10^4 K

Table 2. Parameters for our three different Ly α line profile models

for temperatures between $T = 0.01\text{K}$ and 10^8K .

Our calculations of T_{α} include the Hubble flow and peculiar velocities v_p : outflows (inflows) of gas from a galaxy that correspond to positive (negative) v_p values will redshift (blueshift) the Ly α photons and lead to an increase (decrease) in T_{α} . For each galaxy in a simulation snapshot we derive T_{α} along all directions along the major axes (i.e. along and against the x, y and z axes). By stepping through the simulation box that is divided into 512 cells on the side (and each cell having a size of 461ckpc), we derive the $n_{\text{HI}}(r)$ and $v_p(r)$ profiles from the ASTRAEUS ionisation and vsMDPL density and velocity grids. For any galaxy, we start the profiles at the galaxy position $r_{\text{em}} = 0$ and end them once the highest frequency $x_{\text{max}} = v_{\text{max}}/b = 40$ tracked in our Ly α line profiles has redshifted out of absorption at $r \simeq v_{\text{max}}/[H_0\Omega_m^{1/2}(1+z)^{1/2}] \simeq 13.6/(1+z)^{1/2}\text{cMpc}$. We assume $T_{\text{IGM}} = 10^4\text{K}$ in ionised and $T_{\text{IGM}} = 10^2\text{K}$ in neutral regions. Since the Ly α line redshifts out of resonance very quickly (the light travel time for distance r at $z = 7$ is less than 2 Myrs, shorter than the simulation time steps), a single simulation snapshot suffices for computing the T_{α} values of the galaxies in that snapshot. We also assume periodic boundary conditions when computing T_{α} .

Finally, we derive the observed, i.e. dust and IGM attenuated, Ly α luminosity and line profile along each major axes (resulting in 6 lines of sight) as

$$L_{\alpha,x}(x) = L_{\alpha}^{\text{gal}}(x) T_{\alpha,x}(x) = L_{\alpha}^{\text{intr}} f_{\text{esc}}^{\text{Ly}\alpha} J(x), \quad (61)$$

where $f_{\text{esc}}^{\text{Ly}\alpha}$ and $J(x)$ are the respective Ly α escape fraction and line profile for a one of the models as outlined in Section 3.3.3. The total observed Ly α luminosity L_{α} and total fraction of Ly α radiation transmitted through the IGM are yielded when integrating the respective quantity over the frequency x .

$$L_{\alpha} = \int_{-\infty}^{\infty} L_{\alpha,x}(x) dx \quad (62)$$

$$T_{\alpha} = \int_{-\infty}^{\infty} T_{\alpha,x}(x) dx \quad (63)$$

In the following, we use all lines of sight as independent probes when line-of-sight-sensitive Ly α quantities are analysed.

We derive the observed Ly α luminosities (L_{α}) for all galaxies at $z = 20, 15, 12, 10, 9, 8, 7.3, 7$ and 6.6 for any combination of emerging Ly α line model (*Gaussian*, *Clumpy*, *Porous*) and reionisation scenario (MHDEC, MHCONST, MHINC). Free model parameters (p for the *Gaussian* model, $\tau_{0,\text{cl}}$ for the *Clumpy* and *Porous* models) have been chosen to visually best-fit the observed Ly α LFs at $z \simeq 6.7, 7.0$ and 7.3 (see Tab. 2). For simplicity and better comparison we assume in all models the gas in galaxies to have the temperature of photo-ionised gas, $T = 10^4$ K. Moreover, we note that since the MHCONST scenario represents an intermediate case and provides no further insights, we limit our discussion to the MHDEC and MHINC scenarios in the remainder of this paper.

4 NUMBERS AND PROPERTIES OF $\text{Ly}\alpha$ EMITTING GALAXIES

In this Section, we aim to identify which physical process – the intrinsic $\text{Ly}\alpha$ production (L_{α}^{intr}), the absorption by dust within the galaxies ($f_{\text{esc}}^{\text{Ly}\alpha}$), or the scattering by H I in the IGM (T_{α}) – dominates the observed $\text{Ly}\alpha$ emission. To this end, we analyse (i) how the IGM attenuation profile $T_{\alpha}(x)$ depends on galaxy mass and the f_{esc} -sensitive ionisation topology, (ii) how the $\text{Ly}\alpha$ line profiles emerging from a galaxy depend on the density and velocity distributions of gas and dust within a galaxy and f_{esc} , and how much it affects the fraction of $\text{Ly}\alpha$ radiation that is transmitted through the IGM, and (iii) to which degree the f_{esc} dependency of L_{α}^{intr} , $f_{\text{esc}}^{\text{Ly}\alpha}$, and T_{α} leave characteristic imprints in the $\text{Ly}\alpha$ luminosity functions and the population emitting visible $\text{Ly}\alpha$ emission.

4.1 The transmission through the IGM

We start by discussing the frequency-dependent IGM transmission $T_{\alpha,x}$ shown in the top row of Fig. 3. These profiles depend solely on the underlying ionisation topology and density distribution of the IGM. From the different panels depicting the average $T_{\alpha,x}$ in different halo mass bins of width $\Delta \log_{10} M_h = 0.125$, we see that all $T_{\alpha,x}$ profiles follow a common trend: $T_{\alpha,x}$ decreases towards higher frequencies with an stronger decline around the $\text{Ly}\alpha$ resonance ($x = 0$). Photons bluewards the $\text{Ly}\alpha$ resonance redshift into the $\text{Ly}\alpha$ resonance as they propagate through the IGM and have the largest likelihood to be absorbed by the H I present. Photons redwards the $\text{Ly}\alpha$ resonance are also redshifted, but their likelihood of being absorbed by H I decreases significantly as their energy drops.

In each panel in the top row of Fig. 3 we show $T_{\alpha,x}$ for the two reionisation scenarios MHDEC (yellow/orange/brown lines) and MHINC (blue lines) and redshifts $z = 8.0, 7.3, 7.0, 6.6$ (bright to dark lines as redshift decreases). In general, i.e. for both reionisation scenarios and all halo masses, $T_{\alpha,x}$ increases as the ionised regions grow around galaxies and the IGM is increasingly ionised (bright to dark lines): firstly, a larger ionised region shifts not only the point of strongest $\text{Ly}\alpha$ absorption to higher frequencies x but also reduces the absorption in the damping wings of the $\text{Ly}\alpha$ absorption profile. Secondly, lower H I fractions in ionised regions diminish the number of H I atoms absorbing $\text{Ly}\alpha$ photons.

These two mechanisms shape $T_{\alpha,x}$ redwards and bluewards the $\text{Ly}\alpha$ resonance. As $\text{Ly}\alpha$ photons travel through the IGM and redshift, photons emitted at frequencies $x \gtrsim 0$ see the Gaussian core of the $\text{Ly}\alpha$ absorption profile $\phi(x)$ and are absorbed by H I abundances as low as $\chi_{\text{HI}} \gtrsim 10^{-4}$; thus they are sensitive to the residual H I fraction in ionised regions. Correspondingly, we see in Fig. 3 that $T_{\alpha,x}$ increases for $x \gtrsim 0$ with decreasing redshift as the photoionisation rate around galaxies increases and lowers the residual H I fraction in ionised regions. However, photons emitted at frequencies $x \lesssim 0$ are absorbed by the damping wings of the $\text{Ly}\alpha$ absorption profile $\phi(x)$. Since the $\text{Ly}\alpha$ absorption cross section is lower in the damping wings, the abundance of H I needs to be significantly higher for $\text{Ly}\alpha$ photons to be absorbed; thus, as the sizes of ionised regions decrease, photons emitted at these frequencies are increasingly absorbed by the neutral regions located beyond the ionised regions around the emission sites. For this reason, we find $T_{\alpha,x}$ for $x \lesssim 0$ to increase as the sizes of the ionised regions around galaxies rise with increasing halo mass and decreasing redshift. The rising sizes of ionised regions also become manifest in the shift of the frequency at which $T_{\alpha,x}$ has a value of 0.5 to higher frequencies.

Its dependence on the size of the ionised regions around galax-

ies makes $T_{\alpha,x}$ a tracer of the ionisation topology: our two extreme reionisation scenarios where f_{esc} either increases (MHINC, blue dotted lines) or decreases (MHDEC, yellow to brown solid lines) with rising halo mass M_h exhibit very different ionisation topologies (see Fig. 6). These differences are imprinted in $T_{\alpha,x}$ as follows. Firstly, since in the MHINC scenario the higher f_{esc} values of more massive galaxies ($M_h \gtrsim 10^{10} M_{\odot}$) raise the photoionisation rate within ionised regions (leading to lower χ_{HI} values, also seen in Fig. 2 at $z \lesssim 6$), the corresponding $T_{\alpha,x}$ values are higher bluewards the $\text{Ly}\alpha$ resonance than in the MHDEC scenario. Moreover, in the MHINC scenario, reionisation proceeds faster, leading to the Universe being more ionised at $z < 7$, and the bias of the ionising emissivity towards more massive galaxies grows with time, raising the photoionisation rate in the ionised regions. Both effects contribute to the relative increase in $T_{\alpha,x}$ from MHDEC to MHINC to rise towards lower redshifts bluewards the $\text{Ly}\alpha$ resonance. Secondly, as the size of the ionised regions around galaxies is imprinted in $T_{\alpha,x}$ redwards the $\text{Ly}\alpha$ resonance, MHINC shows lower (higher) $T_{\alpha,x}$ values at $z \gtrsim 7$ ($z \lesssim 7$) than the MHDEC scenario for galaxies with $M_h < 10^{11} M_{\odot}$: At $z \gtrsim 7$, ionised regions become increasingly smaller towards lower mass halos ($M_h \lesssim 10^{9.5} M_{\odot}$) and higher redshifts as the corresponding f_{esc} values and global ionisation fraction decrease. However, at $z \lesssim 7$, this trend reverses as the ionised regions become large enough for the red wing of the $\text{Ly}\alpha$ to be redshifted out of the absorption resonance of the Gaussian core. Towards more massive halos and higher global ionisation fractions, $T_{\alpha,x}$ becomes sensitive to the residual H I fraction in ionised regions (c.f. $T_{\alpha,x}$ in MHINC (light blue dotted line) exceeds $T_{\alpha,x}$ in MHDEC (yellow solid line) at $z = 6.6$). It is interesting to note that the respective $T_{\alpha,x}$ values are very similar in both reionisation scenarios, despite the f_{esc} values of more massive halos ($M_h > 10^{10} M_{\odot}$) differing by about one order of magnitude or more.

4.2 The $\text{Ly}\alpha$ line profiles and luminosity functions

The $\text{Ly}\alpha$ line profile emerging from a galaxy represents a quantity that (i) is shaped by the density and velocity distribution of gas and dust within the galaxy and (ii) affects which fraction of the $\text{Ly}\alpha$ radiation escaping from a galaxy is transmitted through the IGM. In this Section, for our three models of the emerging $\text{Ly}\alpha$ line profiles, we discuss the following: (i) How do the assumed gas and dust distributions affect the attenuation of $\text{Ly}\alpha$ by dust in a galaxy and the emerging $\text{Ly}\alpha$ line profile? (ii) How does the $\text{Ly}\alpha$ line profile affect the $\text{Ly}\alpha$ transmission through the IGM? And, since the luminosity function of the intrinsic $\text{Ly}\alpha$ luminosity (L_{α}^{intr}) will be steeper for the scenario where f_{esc} increases (MHINC) than when it decreases (MHDEC) with rising halo mass, (iii) which characteristics are required for the $\text{Ly}\alpha$ line profiles of the simulated galaxy population to reproduce the observed $\text{Ly}\alpha$ luminosity functions ($\text{Ly}\alpha$ LFs)?

4.2.1 The Gaussian model

The *Gaussian* line model centers the $\text{Ly}\alpha$ line at the $\text{Ly}\alpha$ resonance. The second row in Fig. 3 shows that its width increases as the rotational velocity of a galaxy increases with rising halo mass. Both the increase in the line width and the size of the ionised region surrounding the galaxy lead to higher IGM transmission values of $\text{Ly}\alpha$ radiation as galaxies become more massive (c.f. third row in Fig. 3). At the same time, the fraction of $\text{Ly}\alpha$ photons that escape from the galaxies drops as the abundance of dust increases. We use the ratio between the $\text{Ly}\alpha$ and UV continuum escape fractions to adjust the

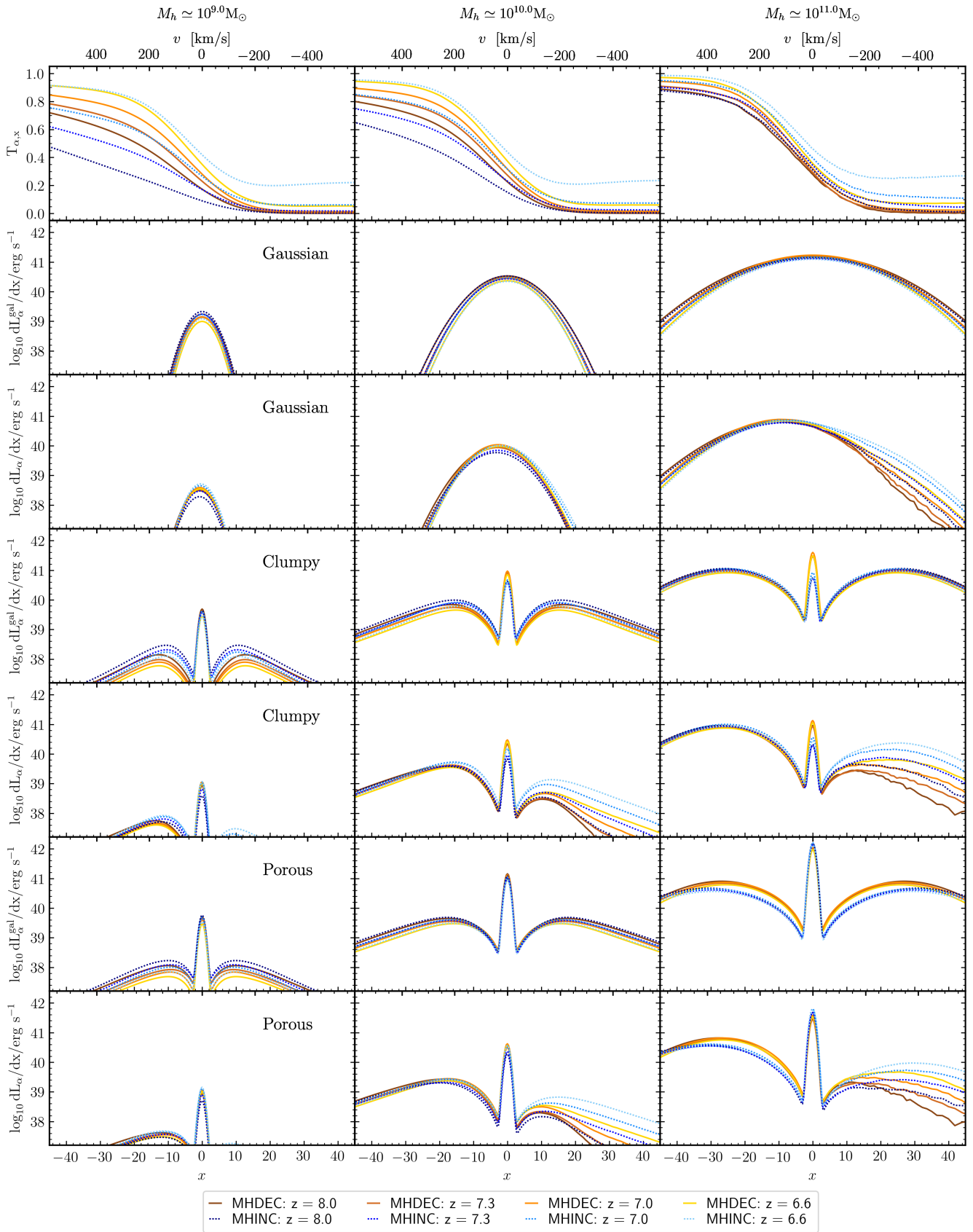


Figure 3. Intrinsic (top) and observed (bottom) Ly α line profile and IGM transmission (centre) at $z = 8.0, 7.3, 7.0, 6.6$ for a homogeneous static gas shell (left), a clumpy gas shell (centre), and a clumpy gas shell with holes through which Ly α radiation escapes without scattering. Solid (dashed dotted) lines show results for the reionisation scenario where f_{esc} decreases (increases) with halo mass M_h .

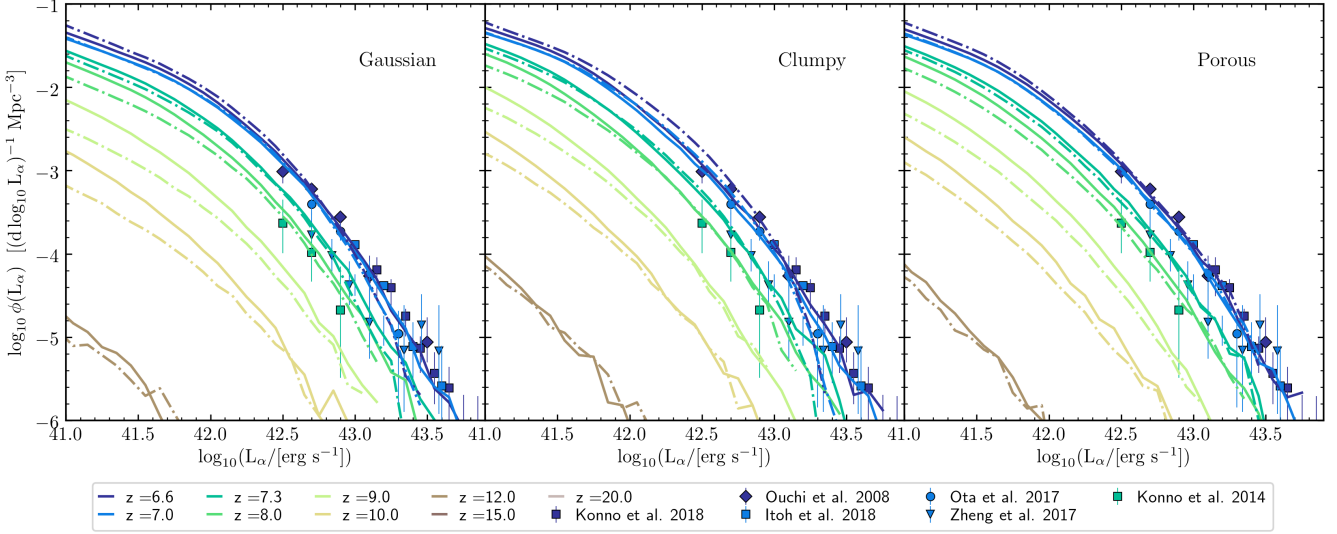


Figure 4. Observed Ly α luminosity functions at $z = 20, 15, 12, 10, 9, 8, 7.3, 7, 6.6$ for a homogeneous static gas shell (left), a clumpy gas shell (centre), and a clumpy gas shell with holes through which Ly α radiation escapes without scattering. Solid (dashed dotted) lines show results for the reionisation scenario where f_{esc} decreases (increases) with halo mass M_h . Observational data points are from Ouchi et al. (2010); Konno et al. (2014); Ota et al. (2017); Zheng et al. (2017); Konno et al. (2018); Itoh et al. (2018).

Ly α luminosities emerging from the galaxies and fit the observed Ly α LFs in each of our reionisation scenarios. In the MHINC scenario the more massive galaxies – that dominate the observed Ly α LF – have higher f_{esc} values than in the MHDEC scenario; to compensate the corresponding lower L_{α}^{intr} values (and steeper slope of the intrinsic Ly α LF), we need a higher $f_{\text{esc}}^{\text{Ly}\alpha}/f_{\text{esc}}^{\text{UV}}$ ratio (1.4) than in the MHDEC scenario (1.0). Despite this compensation, the slopes of the observed Ly α LFs at $z \lesssim 8$ (c.f. left panel in Fig. 4) is still steeper for the MHINC than for the MHDEC scenario.

4.2.2 The Clumpy model

In the *Clumpy* model, the clumpiness of the gas in the shell and the attenuation by dust molecules in these clumps determine the shape of the Ly α line profile. We note that in the following clumpiness describes the number of clumps in the dusty gas shell, i.e. a higher clumpiness corresponds to fewer clumps and thus a higher ratio between the clump ($\tau_{0,\text{cl}}$) and total line optical depth (τ_0). We find the following characteristic trends for the Ly α line profile: Firstly, the clumpier the gas in the shell is, the more Ly α radiation escapes around the Ly α resonance (profile showing a central peak), and the fewer Ly α photons escape through excursion or via the wings (double peak profile). Secondly, when assuming the same clump size for all galaxies – as we do in this paper – the gas clumpiness decreases as galaxies become more massive and contain more gas. Thus, from low-mass to more massive galaxies, we find the Ly α line profile to shift from a central peak dominated to a double-peak dominated profile (see the fourth row in Fig. 3 from left to right), reflecting the transition from the random to the homogeneous regime (see Section 3.1.2). This transition also goes in hand with an increased transmission through the IGM, which we can see when comparing the Ly α profiles emerging from galaxies (fourth row) with those after having traversed the IGM (fifth row in Fig. 3). The Ly α luminosity at $x = 0$ decreases by ~ 0.5 orders of magnitude for all halo masses (from $10^{41.6} \text{ erg s}^{-1}$ to $10^{41.1} \text{ erg s}^{-1}$ for $M_h \simeq 10^{11} M_{\odot}$ and from $10^{39.7} \text{ erg s}^{-1}$ to $10^{39.2} \text{ erg s}^{-1}$ for $M_h \simeq 10^9 M_{\odot}$ for e.g. MHDEC

model), while the peak Ly α luminosity of the red wing decreases only about $\lesssim 0.3$ orders of magnitude at all halo masses. While the blue wing is similarly or more attenuated than the central peak in the IGM, the total fraction of Ly α radiation transmitted through the IGM for a fully-double peaked profile exceeds that of profiles with a central peak component. Furthermore, as the galaxies’ gravitational potentials flatten with decreasing redshift, τ_0 decreases and leads to (i) a narrower double-peak profile (following the dependence of the peak position on $\tau_0^{1/3}$) and (ii) a stronger central peak (the gas becomes clumpier as the ratio $\tau_{0,\text{cl}}/\tau_0$ increases).

A change in the clumpiness of the gas and dust shell (or clump optical depth $\tau_{0,\text{cl}}$ and $\tau_{\text{d,cl}}$) goes not only in hand with a change in the Ly α profile affecting T_{α} but also an altered attenuation of the escaping Ly α radiation by dust. Thus, adjusting the clump optical depth allows us to enhance and reduce the Ly α luminosities and reproduce the observed Ly α LFs: As we increase the size of the clumps, i.e. increase $\tau_{0,\text{cl}}$, Ly α photons will scatter with fewer clumps, leading to (i) a higher fraction $f_{\text{esc}}^{\text{Ly}\alpha}$ escaping, and (ii) a higher fraction escaping at the Ly α resonance, which again leads to stronger attenuation by H I in the IGM. However, we note that once the emerging Ly α profile is fully double-peaked, the attenuation by H I in the IGM can not be further decreased (by changing the injected Ly α line profile). The observable Ly α emission can only be enhanced by decreasing $\tau_{0,\text{cl}}$ as long as the $f_{\text{OH06}}(f_{\text{c,crit}})$ factor in $f_{\text{esc}}^{\text{Ly}\alpha,\text{hom}}$ remains significantly below unity. With the observed Ly α LF being dominated by the more massive galaxies ($M_h \gtrsim 10^{10} M_{\odot}$, as we will discuss in the next Section), we find the $\tau_{0,\text{cl}}$ value to reflect the factor by which the bright end of the intrinsic Ly α LF needs to be reduced to reproduce the observational Ly α LF data points (filled points in Fig. 4). As the intrinsic Ly α LFs is lower at the bright end in the MHINC scenario, a lower $\tau_{0,\text{cl}}$ value (5×10^5) is required than for the MHDEC scenario (1.2×10^6). Nevertheless, the slopes of the resulting observed Ly α LFs at $z \lesssim 8$ keep the trends of the intrinsic Ly α LFs, with the bright ends of the Ly α LFs being steeper in the MHINC than in the MHDEC scenario.

4.2.3 *The Porous model*

The *Porous* model represents a refinement of the *Clumpy* model. It adds gas-free channels through which Ly α and ionising photons escape freely. This explains why, to first order, we find the trends in the last two rows of Fig. 3 to be similar to those in the fourth and fifth rows: a lower clumpiness of gas and dust in the shell induces a stronger prevalence of the double-peak component in the Ly α line profile emerging from a galaxy, enhancing the IGM transmission T_α and absorption by dust within the galaxy, and causing the corresponding Ly α LFs to shift to lower values. On the other hand, it differs from the *Clumpy* model substantially, as f_{esc} determines the minimum fraction of Ly α radiation that escapes at the Ly α resonance and contributes to the central peak in our modelling. Hence, as long as $\tau_{0,\text{cl}}$ remains above the $\tau_{0,\text{cl}}$ value that leads to the same fraction of Ly α escaping in the central peak than given by f_{esc} (referred to as $\tau_{0,\text{cl}}^{\text{crit}}$ in the following), the *Porous* model inherits the trend of the *Clumpy* model. As $\tau_{0,\text{cl}}$ drops below $\tau_{0,\text{cl}}^{\text{crit}}$, a further decrease in $\tau_{0,\text{cl}}$ affects the Ly α line profile emerging from a galaxy hardly, and once the $f_{\text{HO06}}(f_{c,\text{crit}})$ factor of $f_{\text{esc}}^{\text{Ly}\alpha,\text{hom}}$ approaches unity, the observed Ly α LFs remain "fixed". The resulting upper limit of $f_{\text{esc}}^{\text{Ly}\alpha}$ (determined by the total dust optical depth $\tau_{\text{d,total}}$) is essential, as together with L_α^{intr} it provides an upper limit to f_{esc} values that fit the observed Ly α LFs. We find this upper limit to be about $f_{\text{esc}} \sim 0.5$ in our *ASTRAEUS* model.

Due to their opposing dependencies of f_{esc} with halo mass, the Ly α profiles in the *Porous* model show the most noticeable differences between the *MHDEC* and *MHINC* scenarios among our three Ly α line profile models. While the double-peak component is more prominent in the most massive galaxies ($M_h \simeq 10^{11} M_\odot$) in the *MHDEC* scenario, the central peak is slightly stronger in the *MHINC* scenario. To fit the observed Ly α LFs, we find that we require for both reionisation scenarios a more clumpy gas and dust distribution than in the *Clumpy* model, i.e. a (higher) $\tau_{0,\text{cl}}$ value of $1.8 - 2.4 \times 10^6$. These increased $\tau_{0,\text{cl}}$ values enhance the corresponding $f_{c,\text{crit}}$ values and thus the dust attenuation in the homogeneous regime giving rise to the double-peak components and counteract the increased escape close to the Ly α resonance. This model-integrated correlation between $f_{\text{esc}}^{\text{Ly}\alpha}$ and f_{esc} counteracts the trend of flattening (steepening) the slope of the intrinsic Ly α LFs due to f_{esc} decreasing (increasing) with rising halo mass: If f_{esc} is low (high), more (less) Ly α radiation is subject to dust attenuation. This model feature explains why the observed Ly α LFs of the *MHINC* simulation are shallower than in the *Clumpy* model and hardly changes for the *MHDEC* simulation due to its low f_{esc} values for more massive galaxies.

As the dust composition and absorption cross section for Ly α remain highly uncertain during the EoR, we note that a lower (higher) dust absorption cross section κ_{abs} could still reproduce the observed Ly α LFs in our *Clumpy* and *Porous* models by raising (decreasing) the clump optical depth $\tau_{0,\text{cl}}$. However, this would go along with an enhanced (reduced) double-peak and reduced (enhanced) central-peak component in the average Ly α line profile emerging from galaxies.

Finally, we briefly comment on how our emerging and IGM-attenuated Ly α profiles compare to those obtained from radiative hydrodynamical simulations of clouds and small cosmological volumes ($\sim 10^3 \text{cMpc}^3$). While the *Clumpy* and *Porous* reproduce the double- and triple-peak profiles and their dependence on N_{HI} and f_{esc} found in cloud simulations (Kakiichi & Gronke 2021; Kimm et al. 2019, 2022) by construction, their Ly α line profiles differ from those obtained from the *SPHINX* simulation (Garel et al. 2021). In *SPHINX* the median angle-averaged Ly α line profile has been found

z	$\langle \chi_{\text{HI}} \rangle^{\text{MHINC}}$	$\langle \chi_{\text{HI}} \rangle^{\text{MHDEC}}$
8.0	0.84	0.71
7.3	0.69	0.59
7.0	0.52	0.49
6.6	0.23	0.34

Table 3. The evolution of the global H I fractions of the IGM for our reionisation scenarios.

to be less double-peaked towards brighter galaxies, with the blue peak being seemingly increasingly suppressed. This is the opposite trend of our findings. The discrepancy lies in the differently assumed or simulated ISM structures: While our LAE models assume an idealised scenario of same-sized dusty gas clumps, the *SPHINX* simulation follows the formation of star-forming clouds within galaxies. With rising galaxy mass, we expect the simulated *SPHINX* galaxies to contain a higher number of star-forming clouds with various velocity and size distributions. A single or very few star-forming clouds – as found in low-mass galaxies – will give rise to a double-peaked Ly α line profile. Adding the profiles of multiple/many star-forming clouds at different velocities will give rise to increasingly more complex Ly α line profiles as galaxies become more massive. Adjusting our current Ly α line profile models to the complex structure of the ISM will be the subject of future work.

4.3 *The dependence of Ly α properties on halo mass*

In this Section, we provide a more detailed discussion of how the intrinsic Ly α luminosity (L_α^{intr}), the Ly α escape fraction, the Ly α transmission through the IGM, the observed Ly α luminosity, and Ly α equivalent width depend on halo mass and evolve with redshift for the different reionisation scenarios. To this end, we show these quantities as a function of halo mass for both reionisation scenarios (*MHDEC*: yellow/orange/brown lines; *MHINC*: blue lines) and redshifts $z \simeq 8, 7.3, 7, 6.6$ in Fig. 5 and list the corresponding average H I fractions in Table 3. Solid and dot-dashed lines in Fig. 5 depict the median value for galaxies in the given halo mass bin, and shaded regions indicate the range spanned by 68% of the values. For line-of-sight-dependent Ly α properties ($T_\alpha, L_\alpha, \text{EW}_\alpha$), we include all 6 lines of sight.

Intrinsic Ly α luminosity L_α^{intr} : As the most recent star formation dominates the production of ionising photons within galaxies, we find L_α^{intr} to follow the SFR- M_h relation (for a detailed discussion, see Hutter et al. 2021a). While the range of SFR values is broad for low-mass halos ($M_h \lesssim 10^{9.5} M_\odot$) where SN feedback drives stochastic star formation, the SFR- M_h relation becomes tighter towards more massive galaxies as SN feedback ejects an increasingly lower fraction of gas from the galaxy. Being mainly produced by recombining hydrogen atoms within a galaxy, the Ly α radiation produced within the galaxy correlates with the escape fraction of ionising photons as $1 - f_{\text{esc}}$. As we can see from the first row in Fig. 5, this dependency on f_{esc} leads to higher (lower) Ly α luminosities for more massive galaxies, lower (higher) Ly α luminosities for low-mass galaxies, and thus a shallower (steeper) LFs in the *MHDEC* (*MHINC*) scenario.

Ly α escape fraction $f_{\text{esc}}^{\text{Ly}\alpha}$: As the dust content in galaxies increases with their mass, we find $f_{\text{esc}}^{\text{Ly}\alpha}$ to decrease with rising halo mass at all redshifts and for all Ly α line models. However, the different assumed distributions of dust and their resulting attenuation of Ly α radiation lead to differences in the details of this global trend: Firstly, the *Gaussian* model shows a steeper decline in $f_{\text{esc}}^{\text{Ly}\alpha}$ for galaxies with

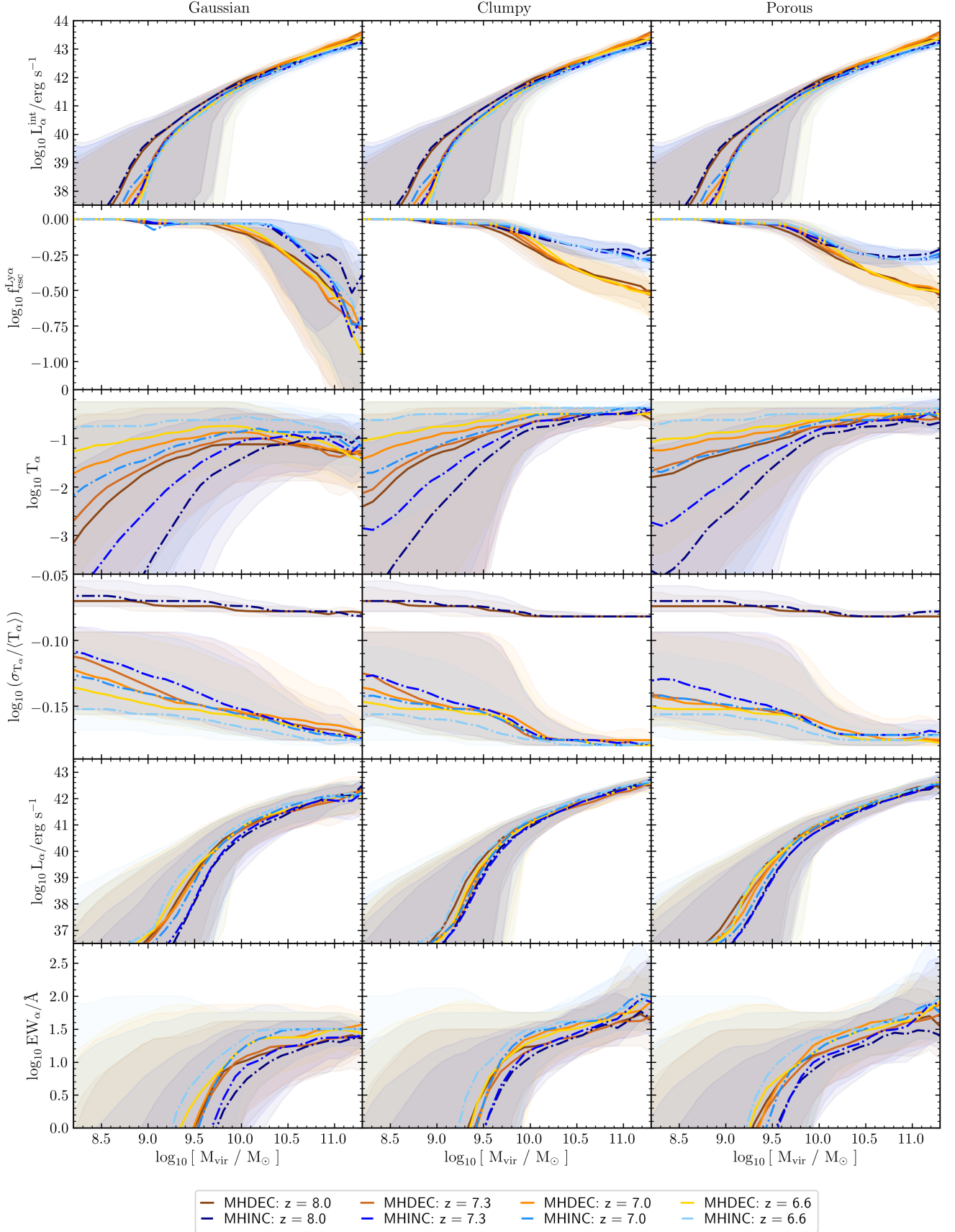


Figure 5. Median of indicated galactic properties (lines) and their $\sim 1.3\sigma$ uncertainties (shaded regions) as a function of halo mass M_h at $z = 8.0, 7.3, 7.0, 6.6$ for a homogeneous static gas shell. Solid (dashed dotted) lines show results for the reionisation scenario where f_{esc} decreases (increases) with halo mass M_h .

$M_h \gtrsim 10^{10.5} M_\odot$ than the *Clumpy* and *Porous* models. Secondly, $f_{\text{esc}}^{\text{Ly}\alpha}$ is always higher in the MHINC than in the MHDEC scenario. This is necessary to reproduce the observed Ly α LFs by compensating the lower intrinsic Ly α luminosities with a more clumpy gas-dust distribution in the MHINC scenario. In case of the *Clumpy* model, it also highlights how a decrease in the clump optical depth by a factor ~ 2 can increase $f_{\text{esc}}^{\text{Ly}\alpha}$ by reducing the fraction of Ly α photons escaping in the homogeneous regime (i.e. a decrease in $f_{\text{c,crit}}$ and $\tau_{0,\text{cl}}$ leads to a reduced number of clumps encounters N_{cl} and the clump albedo ϵ). Thirdly, for the MHDEC (MHINC) scenario, the $f_{\text{esc}}^{\text{Ly}\alpha}$ values show higher (lower) values in the *Porous* model than in the *Clumpy* model for $M_h \lesssim 10^{10} M_\odot$. The reason for this difference is as follows. In both scenarios the higher $\tau_{0,\text{cl}}$ values in the *Porous* model increase the dust attenuation of Ly α escaping in the homogeneous regime. But only a fraction $1 - f_{\text{esc}}$ of the Ly α photons is subject to dust attenuation. This unattenuated escape of Ly α radiation imprints the mass-dependency of f_{esc} in the $f_{\text{esc}}^{\text{Ly}\alpha}$ values. However, for galaxies with $M_h \gtrsim 10^{10} M_\odot$, this imprint ($f_{\text{esc}}^{\text{Ly}\alpha}$ enhancement in *Porous* model) is only visible in the MHINC scenario where f_{esc} values are sufficiently large (> 0.1); in the MHDEC scenario f_{esc} values are too small.

Ly α IGM transmission T_α : As outlined in Section 4.1, the surrounding ionised region (in particular its size and residual H I fraction) and the Ly α line profile emerging from a galaxy determine how much of a galaxy’s escaping Ly α radiation is transmitted through the IGM.

For more massive galaxies with $M_h \gtrsim 10^{10} M_\odot$, T_α is mainly shaped by the Ly α profile. This is because the ionised regions surrounding them are sufficiently large – due to their enhanced ionising emissivity and their clustered neighbourhood – for the Ly α radiation to redshift out of absorption. Hence, at these high halo masses, any trends in T_α reflect the ratio between the Ly α radiation escaping around the Ly α resonance and escaping through the wings: the more Ly α escapes in the central peak, the lower is the T_α value. Indeed, as can be seen in Fig. 5, the *Gaussian* model concentrating the emerging Ly α radiation around the Ly α resonance shows the lowest median T_α values at $M_h \gtrsim 10^{10} M_\odot$ among all Ly α line profile models. In the *Clumpy* model, where the fraction of Ly α escaping through the wings increases with rising halo mass, we find the median T_α value to increase accordingly. This effect is more evident for the MHINC scenario as it transitions from a Ly α line profile with a dominating central peak at $M_h \approx 10^{10} M_\odot$ to one with a prevailing double peak component at $M_h \approx 10^{11} M_\odot$. The *Porous* model also confirms that T_α is highly sensitive to the Ly α line profile. In the MHINC scenario, the double peak component is weaker and increases less with halo mass, leading to slightly lower T_α values than in the *Clumpy* model for $M_h \approx 10^{10-11} M_\odot$ and T_α hardly changing with halo mass. In the MHDEC scenario, we see the same effect but to a lower degree.

However, for less massive galaxies ($M_h \lesssim 10^{10} M_\odot$), T_α is more sensitive to the properties of their surrounding ionised regions. Since the ionised regions around less massive galaxies can differ significantly depending on their environment and phase in their stochastic star formation cycle (see Hutter et al. (2021b) and Legrand et al. (2023) for environment dependence), their T_α values span across an extensive range from as low as effectively zero to as high as $\approx 70\%$. Nevertheless, the median T_α value shows a definite trend. It increases with rising halo mass for all models and at all stages of reionisation. With increasing halo mass, galaxies are surrounded by larger ionised regions as they form more stars emitting ionising photons and are more likely to be located in clustered regions that are reionised ear-

lier. The larger the surrounding ionised regions are, the higher the transmission of Ly α radiation through the IGM. We can see this relationship when comparing the median T_α values of the MHDEC and MHINC simulations. In the MHDEC scenario low-mass galaxies are surrounded by larger ionised regions at $z \gtrsim 7$ than in the MHINC, causing their corresponding T_α values to be raised (c.f. orange/brown solid lines vs dark blue/blue lines in the third row of Fig. 5). At $z \lesssim 7$, however, reionisation progresses faster and the photoionisation rate in clustered ionised regions yields a lower residual H I fraction in the MHINC simulation, both leading to a higher median T_α value for the MHINC than MHDEC scenario at $z \approx 6.6$. Finally, we briefly discuss how the Ly α line profile emerging from a galaxy affects T_α for less massive galaxies. From Fig. 5 we see that the T_α values differ between our three different Ly α line profile models: While at all stages of reionisation the T_α values for $M_h \lesssim 10^{10} M_\odot$ are very similar in the *Porous* and *Clumpy* model, the *Porous* model shows lower T_α values for $M_h \gtrsim 10^{10} M_\odot$ at $z \lesssim 7$ than the *Clumpy* model in the MHINC scenario. This drop goes in hand with the increased central peak component in these more massive galaxies (c.f. Fig. 3 and the previous Section). The median T_α values of the *Gaussian* model always lie below those of the *Clumpy* and *Porous* models; a larger fraction of Ly α radiation escapes closer to the Ly α resonance and is thus subject to stronger attenuation by the IGM.

Variance of the IGM transmission along different lines of sight:

To investigate how strongly the transmission of Ly α radiation through the IGM depends on the direction, we show the standard deviation of T_α values over the 6 lines of sight aligning with the major axes in relation to the corresponding mean value, $\sigma_{T_\alpha}/\langle T_\alpha \rangle = \sqrt{\langle T_\alpha^2 \rangle - \langle T_\alpha \rangle^2} / \langle T_\alpha \rangle$, in the fourth row of Fig. 5. At all redshifts and for all models, $\sigma_{T_\alpha}/\langle T_\alpha \rangle$ decreases with rising halo mass and decreasing redshift for the following reason. As galaxies grow in mass, they produce more ionising photons that can ionise larger regions around them and are also more likely to be located in more strongly clustered ionised regions, both enhancing and homogenising Ly α transmission through the IGM along different lines of sight. However, we note that parts of the decrease of $\sigma_{T_\alpha}/\langle T_\alpha \rangle$ with decreasing redshift is also due to $\langle T_\alpha \rangle$ rising. Since it is hard to disentangle these two effects, we will focus on relative differences between the different reionisation scenarios and Ly α line profile models. Firstly, the more the emerging Ly α line profile is concentrated around the Ly α resonance, the more sensitive is T_α to the varying H I abundance around a galaxy, and the larger is the variance across different lines of sight (c.f. the higher $\sigma_{T_\alpha}/\langle T_\alpha \rangle$ values in the *Gaussian* compared to the other two models, and in the *Porous* compared to the *Clumpy* model for $M_h \gtrsim 10^{10.5} M_\odot$ when central peak component dominates). Secondly, we focus on Ly α line profiles more sensitive to the environmental H I abundance of a galaxy (*Gaussian* model). When accounting for the $\langle T_\alpha \rangle$ values to be lower in the MHINC than in the MHDEC scenario at $z \approx 7$ (see median T_α values in the third row of Fig. 5), we can deduce that the variance of T_α across different lines of sight is higher in the MHDEC than in the MHINC scenario. Indeed in the MHINC scenario, the shape of ionised regions is closer to spheres and less filamentary, which results in more “homogeneous” T_α values.

Observed Ly α luminosity L_α : For any model and reionisation scenario, the trend of L_α with rising halo mass depends on the respective trends of L_α^{intr} , $f_{\text{esc}}^{\text{Ly}\alpha}$, and T_α . Being surrounded by smaller ionised regions, the low T_α values of less massive galaxies ($M_h \lesssim 10^{10} M_\odot$) strongly suppress and shape their emerging Ly α radiation. In contrast, the T_α values of more massive galaxies ($M_h \gtrsim 10^{10} M_\odot$) show only

weak trends with halo mass and similar values throughout reionisation. For this reason, the trends of their L_α values with halo mass are predominantly shaped by the corresponding trends of L_α^{intr} and $f_{\text{esc}}^{\text{Ly}\alpha}$. Though, for model parameters that reproduce the observed Ly α LFs, a relative increase (decrease) of L_α^{intr} towards higher halo masses, such as in the MHINC (MHDEC) scenario, is compensated by an $f_{\text{esc}}^{\text{Ly}\alpha}$ that decreases more (less) strongly with halo mass. Nevertheless, the resulting relation between L_α and halo mass does not significantly change. It shows that only more massive galaxies where SN and radiative feedback do not considerably suppress star formation exhibit observable Ly α emission of $L_\alpha \gtrsim 10^{41} \text{ erg s}^{-1}$.

Observed Ly α equivalent width EW_α : We compute the Ly α equivalent width EW_α from L_α and the observed UV continuum luminosity at 1500\AA (L_c). The trend of the median EW_α with halo mass follows that of L_α , with median EW_α values ranging from $\sim 5 - 30\text{\AA}$ for galaxies in $M_h \simeq 10^{10} M_\odot$ halos to $\sim 25 - 100\text{\AA}$ for galaxies in $M_h \simeq 10^{11.3} M_\odot$ halos. More massive galaxies with a strongly attenuated UV continuum – the fraction of these galaxies increases towards higher halo masses due to the higher abundance of dust – and high L_α values show EW_α values up to $\sim 300\text{\AA}$ in the *Clumpy* and *Porous* models. However, these high EW_α values are not present in the *Gaussian* model for the following reason: in this model, the escape of Ly α and UV continuum radiation differs just by a constant factor, while the dust attenuation of Ly α and UV continuum photons within a galaxy are not only linked via the dust mass in the *Clumpy* and *Porous* models.

In summary, we find that only more massive galaxies ($M_h \gtrsim 10^{10} M_\odot$) where star formation is not substantially suppressed by SN and radiative feedback from reionisation show significant Ly α emission of $L_\alpha \gtrsim 10^{41} \text{ erg s}^{-1}$. This limitation of observable Ly α emission to more massive galaxies allows the f_{esc} -dependency of the intrinsic Ly α luminosity to be compensated by a weaker or stronger attenuation of Ly α by dust within a galaxy. If less massive galaxies were visible in Ly α , they would break this degeneracy as they would not contain enough dust to attenuate the Ly α radiation in all scenarios sufficiently.

5 THE SPATIAL DISTRIBUTION OF LY α EMITTING GALAXIES

In this Section, we analyse where galaxies with observable Ly α emission are located in the large-scale structure and how their environment and Ly α luminosity distributions differ in our reionisation scenarios (MHDEC and MHINC). For this purpose, we discuss the environment of Ly α emitting galaxies in terms of their large-scale spatial distribution (Fig. 6), their surrounding over-density ($1 + \delta$) and H I fraction (χ_{HI}) (Fig. 7), and their 3D autocorrelation functions (Fig. 8). As we yield very similar results for our three Ly α lines profile, we use the *Porous* model as a representative case.

5.1 The environment

Before detailing the location of Ly α emitting galaxies in the large-scale matter distribution, we briefly discuss the ionisation structure of the IGM using Fig. 6 and 7. Fig. 6 shows the ionisation fields at $z = 8, 7$ and 6.7 for the MHDEC (top) and MHINC scenarios (bottom). As can be seen in this Figure, if f_{esc} decreases with halo mass (MHDEC scenario), reionisation is not only more extended but also

ionised regions are on average smaller, follow more the large-scale density distribution and thus have less bubble-like shapes than if f_{esc} increases with halo mass (MHINC scenario). The grey contours in Fig. 7, showing the two-dimensional probability density distribution of the H I fraction (χ_{HI}) and over-density of the IGM at $z = 8, 7.3, 7$ and 6.7 (derived from all cells of the 512^3 ionisation and density grids output by *ASTRAEUS*), complement the picture. These contours indicate that not only an increasing fraction of the volume becomes ionised as reionisation progresses (from right to left) but also the χ_{HI} values in ionised regions decrease (e.g. from $\chi_{\text{HI}} \simeq 10^{-4}$ ($10^{-4.3}$) in average dense regions with $\log_{10}(1 + \delta) + 1$ at $z = 8$ to $\chi_{\text{HI}} \simeq 10^{-4.7}$ ($10^{-5.2}$) at $z = 6.7$ for the MHDEC (MHINC) scenario). The latter is because as galaxies grow in mass with decreasing redshift, their emission of ionising photons increases, leading to a rise of the photoionisation rates within ionised regions and thus lower χ_{HI} values. Moreover, at the same time, as the photoionisation rate within ionised regions becomes increasingly homogeneous, the enhanced number of recombinations in denser regions (for the detailed modelling description see [Hutter 2018](#)) leads to a positive correlation between the H I fraction and density in ionised regions. However, the exact value of the photoionisation rate within ionised regions and its spatial distribution depends strongly on the ionising emissivities escaping from the galaxies into the IGM. If less clustered low-mass galaxies drive reionisation – as in the MHDEC scenario (top row in Fig. 7) –, the resulting photoionisation rate is more homogeneous and lower than if the more strongly clustered massive galaxies are the main drivers of reionisation (c.f. MHINC scenario in the bottom row of Fig. 7). The difference in the photoionisation rate’s magnitude explains the shift of the χ_{HI} values by an order of magnitude to lower values in under-dense to moderately over-dense regions ($\log_{10}(1 + \delta) \lesssim 1.2$) when going from the MHDEC to the MHINC scenario. In contrast, the more inhomogeneous distribution of the photoionisation rate’s values enhances this drop in χ_{HI} in over-dense regions where the most massive galaxies are located.

As we can see from the red stars in Fig. 6 and coloured contours in Fig. 7, galaxies emitting Ly α luminosities of $L_\alpha \geq 10^{42} \text{ erg/s}$ always lie in ionised regions for our Ly α line profile models. Although these galaxies trace the ionisation topology, their populations (and thus locations) hardly differ for our two opposing reionisation scenarios. This absence of a significant difference is due to their massive nature (see also e.g. [Kusakabe et al. 2018](#)): hence, all Ly α emitting galaxies lie in over-dense regions, with the ones brighter in Ly α located in denser regions (c.f. green to blue to red contours). The latter trend is mainly because more massive galaxies, which exhibit higher star formation rates and produce more ionising and Ly α radiation, are located in denser regions.

5.2 The clustering

In this Section, we address the question whether the Ly α luminosity-dependent distribution of LAEs could differ for reionisation scenarios with opposing trends of f_{esc} with halo mass. For this purpose, we analyse the 3D autocorrelation function for LAE samples with different minimum Ly α luminosities (Fig. 8). We define a galaxy to be an LAE if it has an observed Ly α luminosity of $L_\alpha \geq 10^{42} \text{ erg s}^{-1}$.

Before we discuss the differences between our opposing f_{esc} descriptions, we give a brief overview of the global trends and their origins. Firstly, as predicted by hierarchical structure formation, all autocorrelation functions in Fig. 8 decrease from small to large scales, implying stronger clustering of galaxies on small scales than on large scales. Secondly, the dropping amplitude of the LAE autocorrelation functions with decreasing redshift (from ochre to blue lines) reflects

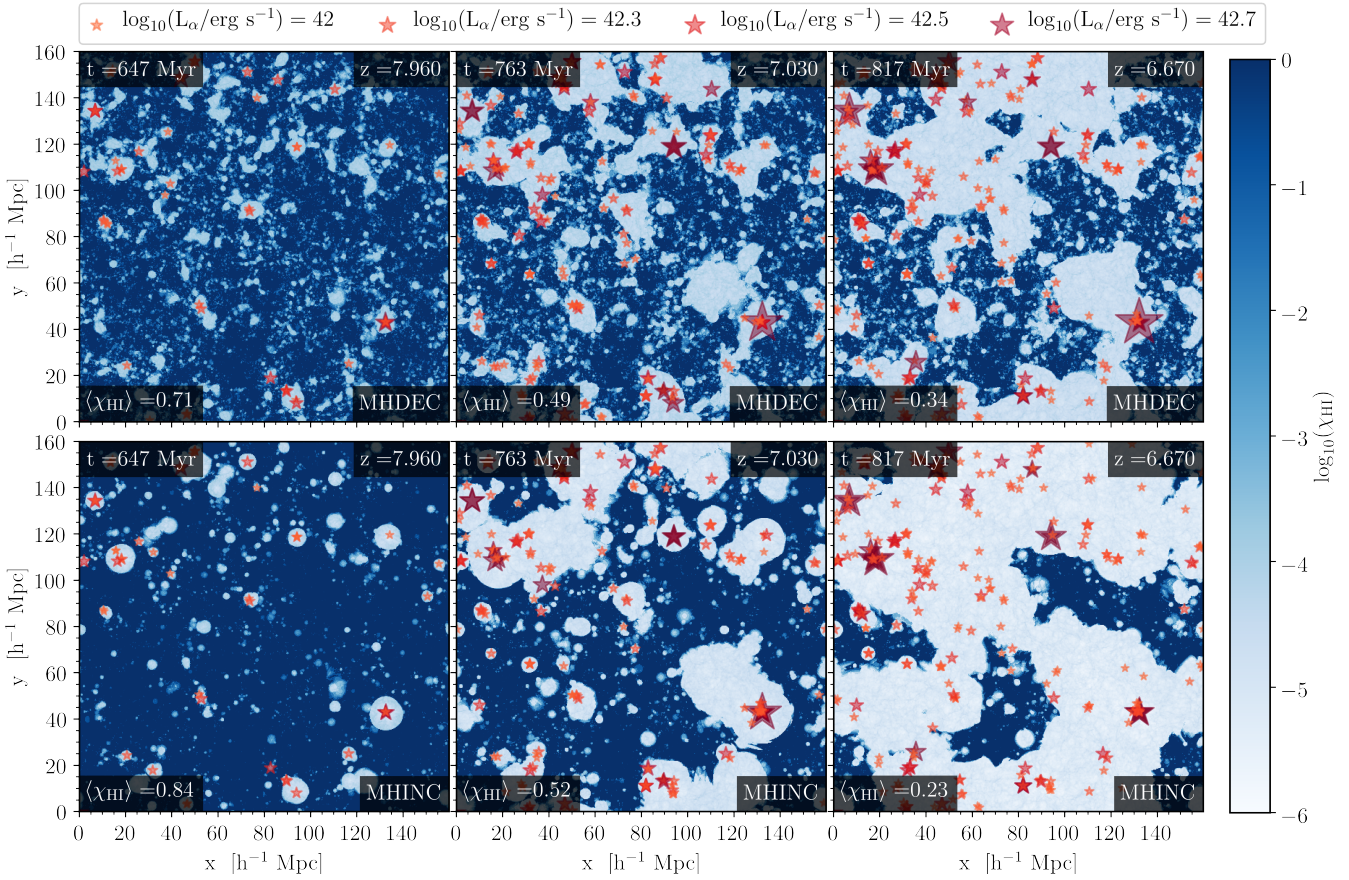


Figure 6. Neutral hydrogen fraction fields at $z = 8.0$ (left), $z = 7.0$ (centre), and $z = 6.6$ (right) for the MHDEC (top) and MHINC Porous models (bottom). We show a $1.6h^{-1}\text{cMpc}$ -thick (5 cells) slice through the centre of the simulation box. The blue color scale depicts the volume-averaged value of the neutral fraction in each cell. Red stars show the location of LAEs, with their sizes and colour scale encoding the observed Ly α luminosity along the z -direction.

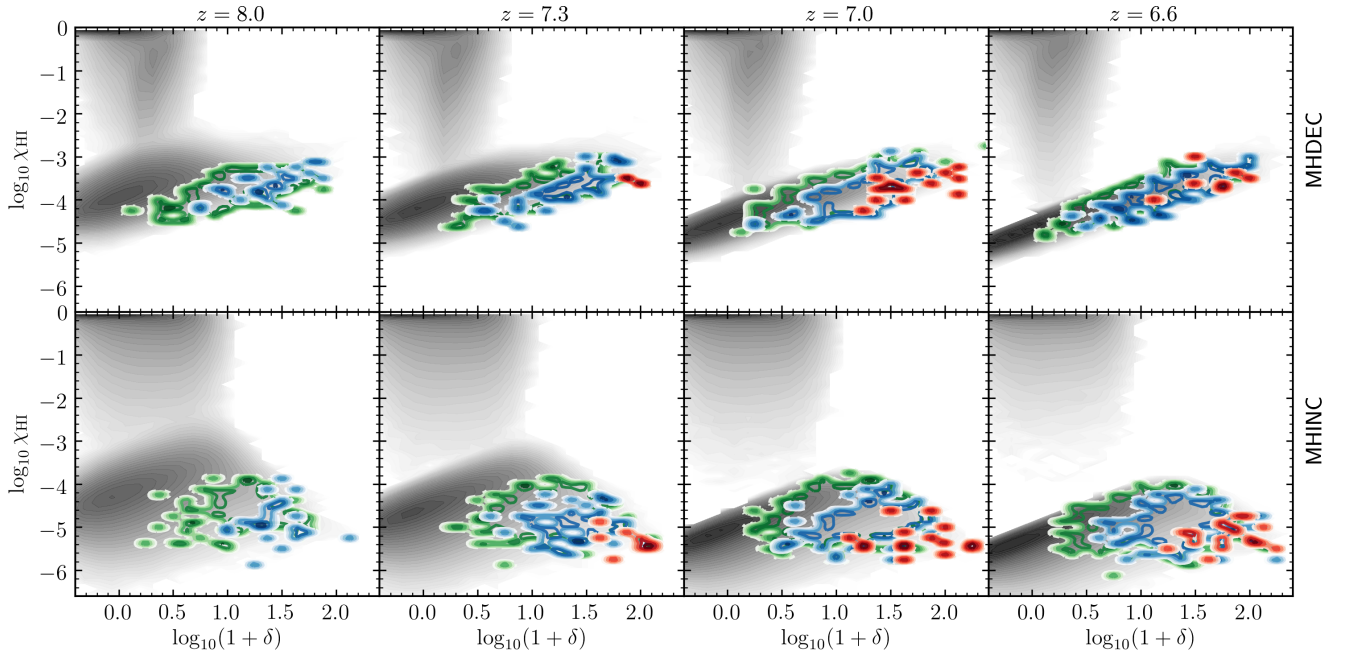


Figure 7. 2D probability distribution in χ_{HI} and overdensity for all simulation cells (grey) and galaxies with $L_{\alpha} \geq 10^{42}\text{erg s}^{-1}$ (green), $L_{\alpha} \geq 10^{42.5}\text{erg s}^{-1}$ (blue), and $L_{\alpha} \geq 10^{43}\text{erg s}^{-1}$ (red) in the Porous model. The top (bottom) row shows results for the reionisation scenario where f_{esc} decreases (increases) with halo mass M_h .

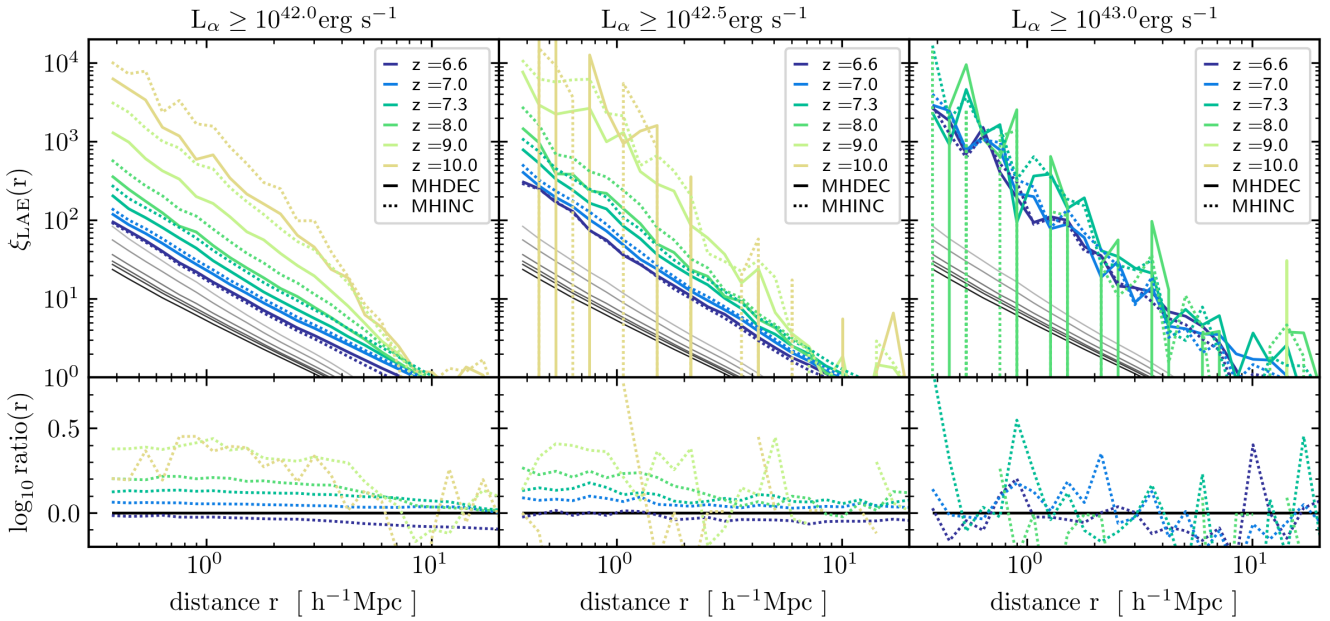


Figure 8. Top panels: 3D correlation function of galaxies that exceed an observed Ly α luminosity of $L_{\alpha} > 10^{42.0} \text{ erg s}^{-1}$ (left), $L_{\alpha} > 10^{42.5} \text{ erg s}^{-1}$ (centre) and $L_{\alpha} > 10^{43.0} \text{ erg s}^{-1}$ (right) at $z = 10, 9, 8, 7.3, 7, 6.6$ for the *Porous* model. Solid (dashed dotted) lines show results for the reionisation scenario where f_{esc} decreases (increases) with halo mass M_h and assumes $\tau_{0,\text{cl}} = 4 \times 10^5$ (2×10^5). The grey to black lines indicate the corresponding LBG ($M_{\text{UV}} < -17$) 3D correlation functions from $z = 10$ to 6.6. Bottom panels: Ratio between the 3D LAE correlation functions of the MHINC and the MHDEC scenario at fixed redshifts.

the growth and increasing ionisation of ionised regions. Thirdly, since the L_{α} value of a galaxy is strongly correlated to its halo mass in our galaxy evolution model, selecting galaxies with increasingly brighter Ly α luminosities (left to right in Fig. 8) corresponds to selecting more massive galaxies. The latter explains the increasing amplitude and stronger clustering. Comparing the correlation functions of the L_{α} selected galaxies with those of LBGs (galaxies with $M_{\text{UV}} \geq -17$) shows that the Ly α selected galaxies are more massive than our LBGs (solid grey lines). It also shows that the decrease in the clustering of LAEs is partially due to galaxies of a given mass becoming a less biased tracer of the underlying density field as the density of the Universe drops with decreasing redshift.

Comparing the autocorrelation functions of our two opposing f_{esc} descriptions, we find that the MHINC scenario (dotted lines) has higher autocorrelation amplitudes than the MHDEC scenario (solid lines) throughout reionisation and for all minimum Ly α luminosities studied. This difference decreases towards larger scales. The reason for these higher amplitudes is twofold: On the one hand, the MHINC scenario has a lower global average ionisation fraction at $z \gtrsim 7$ than the MHDEC scenario (see Fig. 2). Its ionised regions are located around more biased tracers of matter, i.e. more massive galaxies, leading to a stronger clustering. While the scenarios' difference in $\langle \chi_{\text{HI}} \rangle$ reaches its maximum with ~ 0.13 around $z \approx 8$, the difference in the autocorrelation amplitudes rises even towards higher redshifts. This is because, with increasing redshift, galaxies of the same mass become more biased tracers of the underlying matter distribution. Thus, the same difference in $\langle \chi_{\text{HI}} \rangle$ at higher $\langle \chi_{\text{HI}} \rangle$ values leads to a larger difference in the clustering of LAEs, since the Ly α luminosity of a galaxy correlates strongly with its halo mass. We note that selecting LAEs with a higher minimum Ly α luminosity also corresponds to selecting more biased tracers and yields higher correlation amplitudes (c.f. different panels in Fig. 8). On the other hand, during the early stages of reionisation, ionised regions grow preferentially around the most biased tracers of the underlying matter field (most

massive galaxies) in the MHINC scenario. Thus, we would expect that, at the same $\langle \chi_{\text{HI}} \rangle$ value, LAEs in this scenario are more clustered than LAEs in the MHDEC scenario where the f_{esc} decreasing with rising halo mass counteracts the biased growth of ionised regions. Indeed, at $z \lesssim 7$, the correlation amplitude in the MHINC scenario is higher or similar than in the MHDEC scenario, although the Universe is similarly or more ionised in the former, respectively. This difference becomes more apparent as we consider higher minimum Ly α luminosities of $L_{\alpha} > 10^{42.5} \text{ erg s}^{-1}$. It is driven by the higher photoionisation rates in the ionised regions around massive galaxies.

We conclude that, since LAEs coincide with the most massive galaxies located in dense and ionised regions, their clustering is primarily a tracer of the global ionisation state of the IGM. While the exact ionisation topology at fixed $\langle \chi_{\text{HI}} \rangle$ values has only a secondary effect on the clustering of LAEs during the second half of reionisation, the spatial distribution of LAEs provides a relatively robust tool to map the detailed ionisation history at early times.

6 THE RELATION OF LAES TO LBGs

In this Section, we address the question of what defines whether an LBG shows Ly α emission and why the fraction of LBGs with observable Ly α emission changes as the observed UV continuum luminosity (at 1500\AA) or the minimum Ly α equivalent width, EW_{α} , rise. For this purpose, we show both the fraction of LBGs with a Ly α equivalent width of at least $\text{EW}_{\alpha} \geq 25\text{\AA}$ (top row) and $\text{EW}_{\alpha} \geq 50\text{\AA}$ (central row) and the median EW_{α} value (bottom row) as a function of the UV continuum luminosity in Fig. 9.

For our three different Ly α line profile models, we find the median EW_{α} to exhibit similar values of $\sim 4 - 40\text{\AA}$ at all redshifts shown. Furthermore, the EW_{α} values range to lower values as galaxies become UV fainter. As galaxies become less massive, this spread in EW_{α} values reflects the increasingly broader range of star formation

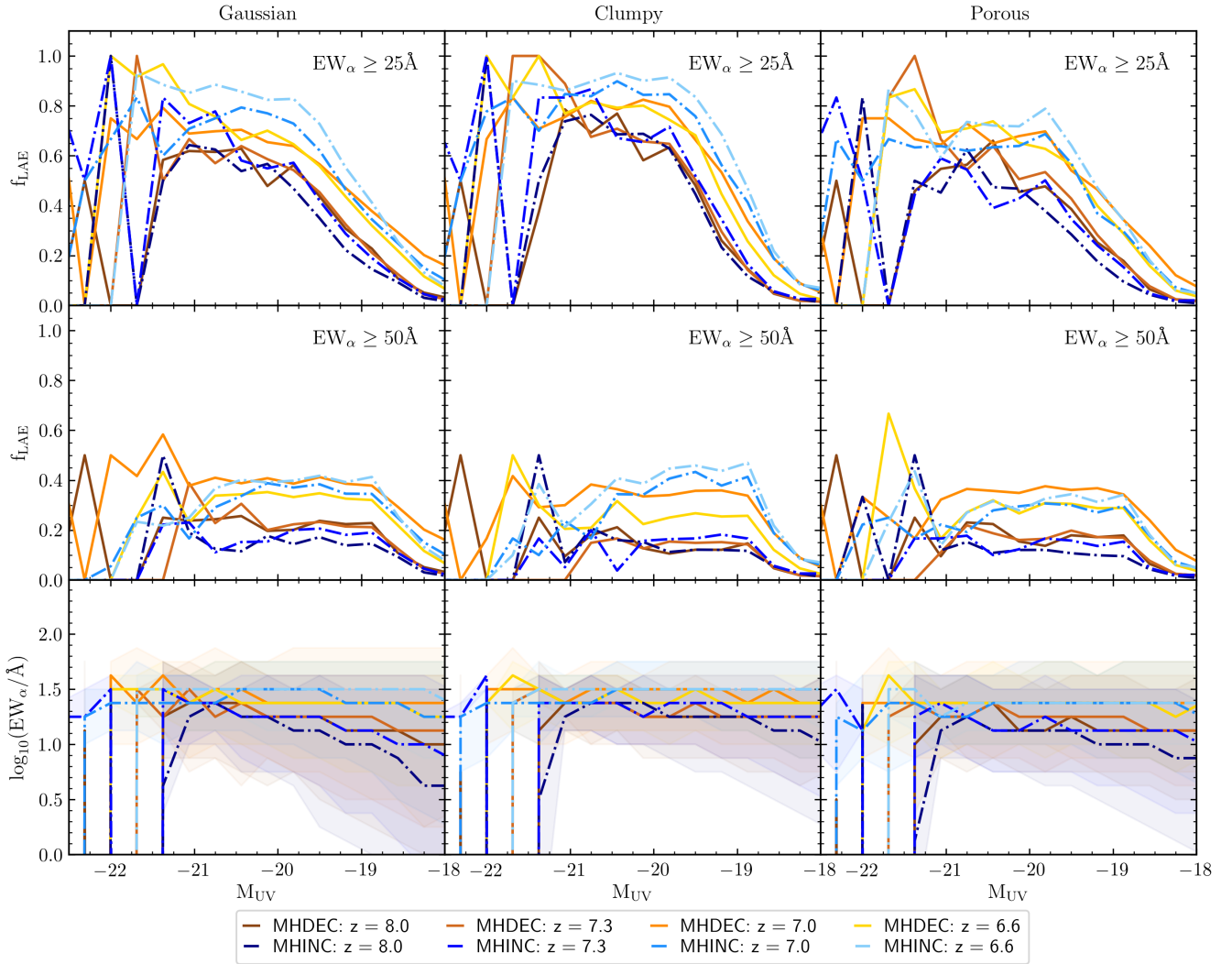


Figure 9. The two top rows depict the fraction of LBGs showing Ly α emissions with $L_{\alpha} \geq 10^{42} \text{erg s}^{-1}$ and EW_{α} exceeding the value marked in the panels for the different Ly α line profile models as marked. The bottom row shows the corresponding medians of the EW_{α} values (lines) and their $\sim 1.3\sigma$ uncertainties (shaded regions). Solid (dashed dotted) lines show results for the reionisation scenario where f_{esc} decreases (increases) with halo mass M_h .

rate values to lower values, which traces back to the larger variety of mass assembly histories that increasingly include progenitors with particularly SN feedback-suppressed star formation. The M_{UV} -dependency of the fraction of LBGs with Ly α emission (f_{LAE}) also reflects this shift towards lower EW_{α} values (c.f. top and central row of Fig. 9): firstly, f_{LAE} decreases towards lower UV luminosities, and secondly, this decrease is stronger for lower than higher EW_{α} cuts. These trends imply that UV bright galaxies are more likely to show higher EW_{α} values for all our Ly α line profile models and reionisation scenarios. For example, while only $< 20\%$ of galaxies with $M_{\text{UV}} \simeq -18$ exceed $\text{EW}_{\alpha} > 25\text{\AA}$, $> 40\%$ of galaxies with $M_{\text{UV}} \gtrsim -20$ exceed $\text{EW}_{\alpha} > 25\text{\AA}$ and $> 5\%$ even $\text{EW}_{\alpha} > 50\text{\AA}$.

Moreover, both the slight rise of EW_{α} and f_{LAE} values with decreasing redshift and their variation among our different reionisation scenarios can be attributed to the increasing fraction of Ly α radiation that is transmitted through the IGM as the Universe becomes more ionised (see T_{α} in Fig. 5). For example, at a given redshift $z > 7$ ($z < 7$), the EW_{α} and f_{LAE} values are on average higher (lower) in the MHDEC than in the MHINC scenario, which is due to a more (less) ionised IGM. Similarly, the lower EW_{α} values reached in the *Gaus-*

sian model for UV fainter galaxies are due to the stronger absorption of Ly α radiation by H I in the IGM. Finally, we note that since in the *Clumpy* and *Porous* models the attenuation of the UV continuum and Ly α by dust do not necessarily correlate with each other (as e.g. parts of Ly α can escape via random walk), a few galaxies that are attenuated strongly in the UV but less in Ly α show high EW_{α} values of $\sim 1000\text{\AA}$. Thus, the main driver of these high EW_{α} values is the dust attenuation of the UV continuum assumed in our models.

Comparing our fraction of LBGs showing Ly α emission with those obtained in observations (e.g. Schenker et al. 2012, 2014; Caruana et al. 2014; Pentericci et al. 2014, 2018; Mason et al. 2019), we find that (i) the observed trend of f_{LAE} decreasing towards higher UV luminosity agrees roughly with our results for $\text{EW}_{\alpha} > 50\text{\AA}$ but not for $\text{EW}_{\alpha} > 25\text{\AA}$, and (ii) our f_{LAE} values are higher than those inferred from observations (again more so for $\text{EW}_{\alpha} > 25\text{\AA}$ than $\text{EW}_{\alpha} > 50\text{\AA}$). These discrepancies hint either at our model predicting too high Ly α or too low UV luminosities (particularly for more massive galaxies) despite reproducing the observed Ly α and UV LFs, or observations missing bright LAEs. Interestingly, we find that the fraction of LBGs with high EW_{α} values

of $f_{\text{LAE}}(\text{EW}_\alpha > 100\text{\AA}) \simeq 1 - 12\%$ and $f_{\text{LAE}}(\text{EW}_\alpha > 240\text{\AA}) \lesssim 1\%$ in the *Clumpy* and *Porous* models are in rough agreement with the results from deep MUSE observations at $z = 3 - 6$ that consider only LAEs with detected UV continuum (Kerutt et al. 2022). A higher abundance of high EW_α values has been found in various high-redshift LAE observations (e.g. Shibuya et al. 2018; Malhotra & Rhoads 2002; Shimasaku et al. 2006). Nevertheless, our f_{LAE} values agree roughly with the results from radiative hydrodynamical simulations post-processed with $\text{Ly}\alpha$ radiative transfer, such as SPHINX (c.f. Fig. B1 in Garel et al. 2021).

7 CONCLUSIONS

We apply our new framework for LAEs to different reionisation scenarios, and analyse how the escape fraction of H I ionising photons, f_{esc} , and its dependence on halo mass affect the luminosity-dependent number and spatial distributions of LAEs. Besides f_{esc} affecting the IGM ionisation topology and the strength of the $\text{Ly}\alpha$ line produced in the ISM, its sensitivity to the density and velocity structure of ISM gas and dust has been found to correlate with the $\text{Ly}\alpha$ line profile emerging from a galaxy and the fraction of $\text{Ly}\alpha$ radiation escaping into the IGM. Notably, the emerging $\text{Ly}\alpha$ line profile reflects the attenuation by dust in the ISM and can also change the fraction of $\text{Ly}\alpha$ radiation that traverses the IGM unattenuated by H I. For this reason, we build an analytical model for $\text{Ly}\alpha$ line profiles that emerge from a $\text{Ly}\alpha$ source surrounded by a shell of dusty gas clumps interspersed with low-density channels. Our model reproduces the numerical radiative transfer results of a shell with dust gas clumps of different sizes as presented in Gronke (2017). By coupling this model to ASTRAEUS, a semi-numerical model coupling galaxy evolution and reionisation self-consistently, we derive the $\text{Ly}\alpha$ line profiles emerging from the simulated galaxy population and explore the resulting large-scale distribution of LAEs for different dependencies of f_{esc} on halo mass (decreasing, constant, increasing) and $\text{Ly}\alpha$ line profiles (Gaussian profile, shell of dusty clumps interspersed with low-density channels or not). For this parameter space, we analyse the resultant ionisation topologies, the dependencies of $\text{Ly}\alpha$ line profiles and $\text{Ly}\alpha$ properties on halo mass, and the location of galaxies with observable $\text{Ly}\alpha$ emission in the large-scale structure. Our main results are the following:

(i) For a shell consisting of clumps of the same size, the $\text{Ly}\alpha$ line profile emerging from a galaxy develops from a central peak at the $\text{Ly}\alpha$ resonance dominated to a double peak dominated profile as it becomes more massive. Adding low-density channels results in either a weakening of this trend, particularly as f_{esc} increases with rising halo mass.

(ii) In all reionisation scenarios and $\text{Ly}\alpha$ line profile models, LAEs (galaxies with $L_\alpha \geq 10^{42} \text{erg s}^{-1}$) are more massive galaxies with $M_h \gtrsim 10^{10} M_\odot$. These galaxies exhibit continuous star formation and are biased tracers of the underlying mass density distribution. Both allow efficient transmission of the $\text{Ly}\alpha$ line through the IGM by facilitating the build-up of ionised regions around them. In contrast, less massive galaxies are surrounded by smaller ionised regions, which results in their $\text{Ly}\alpha$ radiation being significantly attenuated by H I in the IGM.

(iii) As LAEs are more massive galaxies and the most biased tracers of the underlying mass density distribution, they are located in the densest and most highly ionised regions. This finding holds for any inside-out reionisation scenario where dense regions containing massive galaxies are ionised before under-dense voids and for $\text{Ly}\alpha$ line profiles exhibiting emission around/close to the $\text{Ly}\alpha$ resonance

(see also Hutter et al. 2014, 2017). In such scenarios, the spatial distribution of LAEs is primarily sensitive to the global ionisation fraction and only in second-order to the ionisation topology or the trend of f_{esc} with halo mass.

(iv) As the observable $\text{Ly}\alpha$ LFs are composed of the $\text{Ly}\alpha$ emission from more massive galaxies, a decrease in their intrinsic $\text{Ly}\alpha$ luminosities ($\text{Ly}\alpha$ produced in the ISM) due to higher f_{esc} values can be compensated by reducing the attenuation by dust in the ISM (echoing the degeneracy found in Hutter et al. 2014). However, if f_{esc} exceeds ~ 0.5 for the most massive galaxies ($M_h \gtrsim 10^{11} M_\odot$), their intrinsic $\text{Ly}\alpha$ luminosity is too low to reproduce the observed $\text{Ly}\alpha$ LFs (see also Hutter et al. 2014).

All combinations of our reionisation scenarios and $\text{Ly}\alpha$ line profile models result in $\text{Ly}\alpha$ and UV luminosities in reasonable agreement with observational constraints. However, although two of the three $\text{Ly}\alpha$ line profile models investigated use parameterisations of numerical $\text{Ly}\alpha$ radiative transfer simulation results, they represent idealised scenarios where the gas in each galaxy is distributed in clumps of the same mass. In reality, the density and velocity distributions of gas and dust in the ISM are more complex: Firstly, the dusty gas clumps will have different masses, with a distribution close to that of a scale-free one at the massive end. Such a mass distribution would result in more massive galaxies having larger clumps than less massive galaxies, which again would lead to a homogenisation of their $\text{Ly}\alpha$ line profiles where more massive (less massive) galaxies have an enhanced (weakened) central peak component and a weakened (enhanced) double-peak component. This change in the $\text{Ly}\alpha$ line profiles would result in the $\text{Ly}\alpha$ radiation being less (more) attenuated by dust in the ISM and traversing the IGM more (less) efficiently. Secondly, the medium between the clumps as well as the low-density channels might not be fully ionised (and very unlikely to be gas-free), causing the $\text{Ly}\alpha$ radiation escaping close to its resonance (central peak used in this work) to contribute to a narrower double-peak profile. Additionally, the gas may exhibit a turbulent velocity structure that could broaden the double-peak component. Both partially neutral low-density channels and an inhomogeneous velocity structure are likely to enhance the transmission of $\text{Ly}\alpha$ through the IGM. Thirdly, the attenuation of $\text{Ly}\alpha$ radiation by dust in the ISM depends on the distribution of dust in clumps. While our model assumes that gas and dust are perfectly mixed, a scenario where dust condensates in the centre surrounded by a shell of hydrogen gas would lower the absorption probability per clump and enhance the escape fraction of $\text{Ly}\alpha$ photons from a galaxy. Finally, simulations and observations of local analogues of high-redshift galaxies (i.e. regarding their extreme metallicity and ionisation continuum properties) indicate that stellar feedback, especially that of supernovae, heat the gas and drive gas outflows (e.g. Gronke & Oh 2020; Kakiichi & Gronke 2021; Carr et al. 2021; Fielding & Bryan 2022; Xu et al. 2023; Hu et al. 2023). Indeed expanding homogeneous shell models have been used to fit observed $\text{Ly}\alpha$ profiles from high-redshift analogues (e.g. Gronke 2017; Orlitová et al. 2018), however, the inferred outflow velocities are on average lower than those inferred from ultraviolet absorption lines of low-ionisation-state elements (Orlitová et al. 2018; Xu et al. 2023), hinting at more complex outflow geometries and kinematics of the neutral gas (see e.g. Carr et al. 2021; Blaizot et al. 2023). In general, outflowing neutral gas causes the $\text{Ly}\alpha$ photons to redshift, enabling easier escape from the galaxy and transmission through the IGM. While in principle outflows could enhance the observed $\text{Ly}\alpha$ emission, particularly from low-mass ($M_h \lesssim 10^{10} M_\odot$) galaxies, and make the large-scale LAE distribution more sensitive to the ionisation topology, their velocities or neutral gas fraction might be not

sufficient to redshift the Ly α radiation out of absorption. In future work, we will extend our analytical Ly α line models towards more realistic outflow geometries and kinematics and explore whether this will affect the large-scale LAE distribution during reionisation significantly.

Our Ly α line profile models, despite being limited by the simplified structure assumed for the ISM, represent a first step towards more complex analytical models for the Ly α line emerging from galaxies that are computationally efficient enough to derive the Ly α emitter populations in large cosmological simulations. To date, many models deriving the large-scale distribution of LAEs assume Ly α line profiles that arise from outflowing gas, consisting of a dominant red and a negligible blue peak (Mesinger et al. 2015; Mason et al. 2018; Weinberger et al. 2019). However, such profiles are hardly seen in Ly α radiative transfer simulations of simulated galaxies (see e.g. Laursen et al. 2011; Garel et al. 2021; Blaizot et al. 2023).

Finally, our finding that the spatial distribution of LAEs is not sensitive to the dependence of f_{esc} with halo mass suggests that LAEs alone can not help to constrain any gradual dependence of f_{esc} with galactic properties. Any dependency introduced in the intrinsic Ly α luminosity can be compensated by the opposed trend of the Ly α escape fraction, achieved by changing the ISM gas and dust distribution. This insensitivity to f_{esc} dependencies makes LAEs relatively robust tracers of the underlying density field that we can use to pin down the ionisation topology. Constraining f_{esc} during the EoR will require a combination of ionisation topology measurements through the H I 21cm signal and measurements of other emission lines.

ACKNOWLEDGEMENTS

We thank Max Gronke and Peter Laursen for useful discussions and the anonymous referee for their comments. AH, GY, LL, PD and SG acknowledge support from the European Research Council's starting grant ERC StG-717001 ("DELPHI"). AH, MT, PD also acknowledge support from the NWO grant 016.VIDI.189.162 ("ODIN") and the European Commission's and University of Groningen's CO-FUND Rosalind Franklin program. AH acknowledges support by the VILLUM FONDEN under grant 37459. PD thanks the Institute for Advanced Study (IAS) Princeton, where a part of this work was carried out, for their generous hospitality and support through the Bershadsky Fund. GY acknowledges financial support from MI-CIU/FEDER under project grant PGC2018-094975-C21. We thank Peter Behroozi for creating and providing the ROCKSTAR merger trees of the vsMDPL and esMDPL simulations. The authors wish to thank V. Springel for allowing us to use the L-Gadget2 code to run the different Multidark simulation boxes, including the vsMDPL and esMDPL used in this work. The vsMDPL and esMDPL simulations have been performed at LRZ Munich within the project pr87yi. The authors gratefully acknowledge the Gauss Centre for Supercomputing e.V. (www.gauss-centre.eu) for funding this project by providing computing time on the GCS Supercomputer SUPERMUC-NG at Leibniz Supercomputing Centre (www.lrz.de). The CosmoSim database (www.cosmosim.org) provides access to the simulations and the Rockstar data. The database is a service by the Leibniz Institute for Astrophysics Potsdam (AIP). The Cosmic Dawn Center (DAWN) is funded by the Danish National Research Foundation under grant No. 140. This research made use of matplotlib, a Python library for publication quality graphics (Hunter 2007); and the Python library numpy (Oliphant 2006).

DATA AVAILABILITY

The source code of the semi-numerical galaxy evolution and reionisation model within the ASTRAEUS framework is available on GitHub (<https://github.com/annehutter/astraeus>). The underlying N-body DM simulation, the ASTRAEUS simulations and derived data in this research will be shared on reasonable request to the corresponding author.

REFERENCES

- Adams T. F., 1975, *ApJ*, 201, 350
- Anderson L., Governato F., Karcher M., Quinn T., Wadsley J., 2017, *MNRAS*, 468, 4077
- Asano R. S., Takeuchi T. T., Hirashita H., Inoue A. K., 2013, *Earth, Planets and Space*, 65, 213
- Behroozi P. S., Wechsler R. H., Wu H.-Y., 2013a, *ApJ*, 762, 109
- Behroozi P. S., Wechsler R. H., Busha M. T., Klypin A. A., Primack J. R., 2013b, *ApJ*, 763, 18
- Blaizot J., et al., 2023, *MNRAS*, 523, 3749
- Bosman S. E. I., et al., 2022, *MNRAS*, 514, 55
- Carr C., Scarlata C., Henry A., Panagia N., 2021, *ApJ*, 906, 104
- Caruana J., Bunker A. J., Wilkins S. M., Stanway E. R., Lacy M., Jarvis M. J., Lorenzoni S., Hickey S., 2012, *MNRAS*, 427, 3055
- Caruana J., Bunker A. J., Wilkins S. M., Stanway E. R., Lorenzoni S., Jarvis M. J., Ebert H., 2014, *MNRAS*, 443, 2831
- Castellano M., et al., 2016, *ApJ*, 818, L3
- Castellano M., et al., 2018, *ApJ*, 863, L3
- Chardin J., Aubert D., Ocvirk P., 2012, *A&A*, 548, A9
- Chen Z., Xu Y., Wang Y., Chen X., 2019, *ApJ*, 885, 23
- Cole S., Lacey C. G., Baugh C. M., Frenk C. S., 2000, *MNRAS*, 319, 168
- Dayal P., Maselli A., Ferrara A., 2011, *MNRAS*, 410, 830
- Dayal P., Ferrara A., Dunlop J. S., Pacucci F., 2014, *MNRAS*, 445, 2545
- Dayal P., et al., 2022, *MNRAS*, 512, 989
- Dijkstra M., Gronke M., Venkatesan A., 2016, *ApJ*, 828, 71
- Endsley R., Stark D. P., 2022, *MNRAS*, 511, 6042
- Endsley R., et al., 2022, *MNRAS*, 517, 5642
- Fan X., et al., 2006, *AJ*, 132, 117
- Faucher-Giguère C.-A., Kereš D., Dijkstra M., Hernquist L., Zaldarriaga M., 2010, *ApJ*, 725, 633
- Ferrara A., Loeb A., 2013, *MNRAS*, 431, 2826
- Fielding D. B., Bryan G. L., 2022, *ApJ*, 924, 82
- Forero-Romero J. E., Yepes G., Gottlöber S., Knollmann S. R., Cuesta A. J., Prada F., 2011, *MNRAS*, 415, 3666
- Fuller S., et al., 2020, *ApJ*, 896, 156
- Furlanetto S. R., Oh S. P., 2016, *MNRAS*, 457, 1813
- Galliano F., 2022, Habilitation Thesis, p. 1
- Garaldi E., Kannan R., Smith A., Springel V., Pakmor R., Vogelsberger M., Hernquist L., 2022, *MNRAS*, 512, 4909
- Garel T., Blaizot J., Rosdahl J., Michel-Dansac L., Haehnelt M. G., Katz H., Kimm T., Verhamme A., 2021, *MNRAS*, 504, 1902
- Gazagnes S., Chisholm J., Schaerer D., Verhamme A., Izotov Y., 2020, *A&A*, 639, A85
- Gnedin N. Y., 2000, *ApJ*, 542, 535
- Gnedin N. Y., Kaurov A. A., 2014, *ApJ*, 793, 30
- Gronke M., 2017, *A&A*, 608, A139
- Gronke M., Oh S. P., 2020, *MNRAS*, 494, L27
- Hansen M., Oh S. P., 2006, *MNRAS*, 367, 979
- He C.-C., Ricotti M., Geen S., 2020, *MNRAS*, 492, 4858
- Heckman T. M., et al., 2011, *ApJ*, 730, 5
- Howard C. S., Pudritz R. E., Harris W. E., Klessen R. S., 2018, *MNRAS*, 475, 3121
- Hu E. M., Cowie L. L., Songaila A., Barger A. J., Rosenwasser B., Wold I. G. B., 2016, *ApJ*, 825, L7
- Hu W., et al., 2021, *Nature Astronomy*, 5, 485
- Hu W., et al., 2023, *arXiv e-prints*, p. arXiv:2307.04911
- Hunter J. D., 2007, *Computing In Science & Engineering*, 9, 90

- Hutter A., 2018, *MNRAS*, **477**, 1549
- Hutter A., Dayal P., Partl A. M., Müller V., 2014, *MNRAS*, **441**, 2861
- Hutter A., Dayal P., Müller V., 2015, *MNRAS*, **450**, 4025
- Hutter A., Dayal P., Müller V., Trott C. M., 2017, *ApJ*, **836**, 176
- Hutter A., Watkinson C. A., Seiler J., Dayal P., Sinha M., Croton D. J., 2020, *MNRAS*, **492**, 653
- Hutter A., Dayal P., Yepes G., Gottlöber S., Legrand L., Ucci G., 2021a, *MNRAS*, **503**, 3698
- Hutter A., Dayal P., Legrand L., Gottlöber S., Yepes G., 2021b, *MNRAS*, **506**, 215
- Itoh R., et al., 2018, *ApJ*, **867**, 46
- Jaskot A. E., Dowd T., Oey M. S., Scarlata C., McKinney J., 2019, *ApJ*, **885**, 96
- Jensen H., Laursen P., Mellema G., Iliev I. T., Sommer-Larsen J., Shapiro P. R., 2013, *MNRAS*, **428**, 1366
- Jung I., et al., 2020, *ApJ*, **904**, 144
- Kakiichi K., Gronke M., 2021, *ApJ*, **908**, 30
- Kashikawa N., et al., 2011, *ApJ*, **734**, 119
- Keating L. C., Weinberger L. H., Kulkarni G., Haehnelt M. G., Chardin J., Aubert D., 2020, *MNRAS*, **491**, 1736
- Kerutt J., et al., 2022, *A&A*, **659**, A183
- Kim H.-S., Wyithe J. S. B., Park J., Lacey C. G., 2013, *MNRAS*, **433**, 2476
- Kim J.-G., Kim W.-T., Ostriker E. C., 2019, *ApJ*, **883**, 102
- Kimm T., Cen R., 2014, *ApJ*, **788**, 121
- Kimm T., Katz H., Haehnelt M., Rosdahl J., Devriendt J., Slyz A., 2017, *MNRAS*, **466**, 4826
- Kimm T., Blaizot J., Garel T., Michel-Dansac L., Katz H., Rosdahl J., Verhamme A., Haehnelt M., 2019, *MNRAS*, **486**, 2215
- Kimm T., Bieri R., Geen S., Rosdahl J., Blaizot J., Michel-Dansac L., Garel T., 2022, *ApJS*, **259**, 21
- Kobayashi C., Karakas A. I., Lugaro M., 2020, *ApJ*, **900**, 179
- Konno A., et al., 2014, *ApJ*, **797**, 16
- Konno A., et al., 2018, *PASJ*, **70**, S16
- Kusakabe H., et al., 2018, *PASJ*, **70**, 4
- Laursen P., 2010, PhD thesis, Niels Bohr Institute for Astronomy, Physics and Geophysics
- Laursen P., Sommer-Larsen J., Razoumov A. O., 2011, *ApJ*, **728**, 52
- Laursen P., Sommer-Larsen J., Milvang-Jensen B., Fynbo J. P. U., Razoumov A. O., 2019, *A&A*, **627**, A84
- Legrand L., Dayal P., Hutter A., Gottlöber S., Yepes G., Trebitsch M., 2023, *MNRAS*, **519**, 4564
- Leitherer C., et al., 1999, *ApJS*, **123**, 3
- Lewis J. S. W., et al., 2020, *MNRAS*,
- Lisenfeld U., Ferrara A., 1998, *ApJ*, **496**, 145
- Malhotra S., Rhoads J. E., 2002, *ApJ*, **565**, L71
- Malhotra S., Rhoads J. E., 2004, *ApJ*, **617**, L5
- Maoz D., Mannucci F., Brandt T. D., 2012, *MNRAS*, **426**, 3282
- Mason C. A., Treu T., Dijkstra M., Mesinger A., Trenti M., Pentericci L., de Barros S., Vanzella E., 2018, *ApJ*, **856**, 2
- Mason C. A., et al., 2019, *MNRAS*, **485**, 3947
- Matthee J., Sobral D., Gronke M., Paulino-Afonso A., Stefanon M., Röttgering H., 2018, *A&A*, **619**, A136
- McKee C., 1989, in Allamandola L. J., Tielens A. G. G. M., eds, IAU Symposium Vol. 135, Interstellar Dust. p. 431
- McQuinn M., Hernquist L., Zaldarriaga M., Dutta S., 2007, *MNRAS*, **381**, 75
- Mesinger A., Aykutaalp A., Vanzella E., Pentericci L., Ferrara A., Dijkstra M., 2015, *MNRAS*, **446**, 566
- Meyer R. A., Laporte N., Ellis R. S., Verhamme A., Garel T., 2021, *MNRAS*, **500**, 558
- Mo H. J., Mao S., White S. D. M., 1998, *MNRAS*, **295**, 319
- Neufeld D. A., 1990, *ApJ*, **350**, 216
- Ocvirk P., et al., 2016, *MNRAS*, **463**, 1462
- Ocvirk P., et al., 2020, *MNRAS*, **496**, 4087
- Oesch P. A., et al., 2015, *ApJ*, **804**, L30
- Olyphant T., 2006, NumPy: A guide to NumPy, USA: Trelgol Publishing, <http://www.numpy.org/>
- Ono Y., et al., 2012, *ApJ*, **744**, 83
- Orlitová I., Verhamme A., Henry A., Scarlata C., Jaskot A., Oey M. S., Schaerer D., 2018, *A&A*, **616**, A60
- Ota K., et al., 2010, *ApJ*, **722**, 803
- Ota K., et al., 2017, *ApJ*, **844**, 85
- Ouchi M., et al., 2010, *ApJ*, **723**, 869
- Padovani P., Matteucci F., 1993, *ApJ*, **416**, 26
- Pentericci L., et al., 2011, *ApJ*, **743**, 132
- Pentericci L., et al., 2014, *ApJ*, **793**, 113
- Pentericci L., et al., 2018, *A&A*, **619**, A147
- Planck Collaboration et al., 2020, *A&A*, **641**, A6
- Qin Y., Wyithe J. S. B., Oesch P. A., Illingworth G. D., Leonova E., Mutch S. J., Naidu R. P., 2022, *MNRAS*, **510**, 3858
- Roberts-Borsani G. W., et al., 2016, *ApJ*, **823**, 143
- Salpeter E. E., 1955, *ApJ*, **121**, 161
- Schenker M. A., Stark D. P., Ellis R. S., Robertson B. E., Dunlop J. S., McLure R. J., Kneib J.-P., Richard J., 2012, *ApJ*, **744**, 179
- Schenker M. A., Ellis R. S., Konidaris N. P., Stark D. P., 2014, *ApJ*, **795**, 20
- Seiler J., Hutter A., Sinha M., Croton D., 2019, *MNRAS*, **487**, 5739
- Shibuya T., et al., 2018, *PASJ*, **70**, S14
- Shimasaku K., et al., 2006, *PASJ*, **58**, 313
- Sobacchi E., Mesinger A., 2015, *MNRAS*, **453**, 1843
- Songaila A., Hu E. M., Barger A. J., Cowie L. L., Hasinger G., Rosenwasser B., Waters C., 2018, *ApJ*, **859**, 91
- Springel V., 2005, *MNRAS*, **364**, 1105
- Tilvi V., et al., 2020, *ApJ*, **891**, L10
- Todini P., Ferrara A., 2001, *MNRAS*, **325**, 726
- Totani T., Kawai N., Kosugi G., Aoki K., Yamada T., Iye M., Ohta K., Hattori T., 2006, *PASJ*, **58**, 485
- Totani T., et al., 2014, *PASJ*, **66**, 63
- Treu T., Trenti M., Stiavelli M., Auger M. W., Bradley L. D., 2012, *ApJ*, **747**, 27
- Triani D. P., Sinha M., Croton D. J., Pacifici C., Dwek E., 2020, *MNRAS*, **493**, 2490
- Ucci G., et al., 2023, *MNRAS*, **518**, 3557
- Vanzella E., et al., 2011, *ApJ*, **730**, L35
- Verhamme A., Orlitová I., Schaerer D., Hayes M., 2015, *A&A*, **578**, A7
- Verhamme A., Orlitová I., Schaerer D., Izotov Y., Worseck G., Thuan T. X., Guseva N., 2017, *A&A*, **597**, A13
- Weinberger L. H., Kulkarni G., Haehnelt M. G., Choudhury T. R., Puchwein E., 2018, *MNRAS*, **479**, 2564
- Weinberger L. H., Haehnelt M. G., Kulkarni G., 2019, *MNRAS*, **485**, 1350
- Wise J. H., Demchenko V. G., Halicek M. T., Norman M. L., Turk M. J., Abel T., Smith B. D., 2014, *MNRAS*, **442**, 2560
- Xu H., Wise J. H., Norman M. L., Ahn K., O'Shea B. W., 2016, *ApJ*, **833**, 84
- Xu X., et al., 2023, *arXiv e-prints*, p. arXiv:2301.11498
- Yates R. M., Henriques B., Thomas P. A., Kauffmann G., Johansson J., White S. D. M., 2013, *MNRAS*, **435**, 3500
- Zheng Z.-Y., et al., 2017, *ApJ*, **842**, L22
- Zhu Y., et al., 2021, *ApJ*, **923**, 223
- Zitrin A., et al., 2015, *ApJ*, **810**, L12

APPENDIX A: GEOMETRICAL CORRECTION FACTOR ξ

When deriving the attenuation of the UV continuum by dust, we have assumed the light sources and dust to be homogeneously distributed within a slab. However, the numerical Ly α radiative transfer simulations in Gronke (2017) assume a screen of dust and gas between the light sources and the observer. To make the escape fractions of the UV continuum and Ly α radiation consistent, we introduce a geometrical correction factor that adjusts the Ly α escape fraction for sources behind a screen to that for sources distributed in a dusty gas slab. According to Forero-Romero et al. (2011), the Ly α escape fraction

relations for these two geometries are given by

$$f_{\text{esc}}^{\text{screen}}(\tau_0) = \frac{1}{\cosh\left(\xi_0 \sqrt{(a\tau_0)^{1/3} \tau_a}\right)} \quad (\text{A1})$$

$$f_{\text{esc}}^{\text{slab}}(\tau_0) = \frac{1 - \exp(-P)}{P} \quad (\text{A2})$$

$$P = \epsilon_0 \left((a\tau_0)^{1/3} \tau_a \right)^{3/4} \quad (\text{A3})$$

$$\tau_a = \tau_{\text{d,total}}(1 - A), \quad (\text{A4})$$

where A is the albedo. By equating the expressions for the Ly α escape fractions,

$$f_{\text{esc}}^{\text{screen}}(\tau_0^{\text{eff}}) = f_{\text{esc}}^{\text{slab}}(\tau_0), \quad (\text{A5})$$

we derive a correction factor ξ that reduces the H I column density in the screen geometry to the slab geometry.

$$\xi = \frac{\tau_0^{\text{eff}}}{\tau_0} = \min\left(\xi_{\text{max}}, \frac{\epsilon_0}{\xi_0^{3/2}} \frac{\left(\text{arcosh}\left(\frac{P}{1 - e^{-P}}\right)\right)^{3/2}}{P}\right) \quad (\text{A6})$$

$$P = \epsilon_0 a^{1/4} \left((1 - A) \frac{M_{\text{d}}}{M_{\text{HI}}} \frac{\kappa_{\text{abs}} m_{\text{H}}}{\sigma_{\text{HI}}} \right)^{3/4} \tau_0 \quad (\text{A7})$$

Here we assume $A = 0.5$ and $\xi_0 = 2.48$, with ξ_0 being adjusted to reproduce $f_{\text{esc}}^{\text{screen}}$ shown in Fig. 1 in [Forero-Romero et al. \(2011\)](#). $\xi_{\text{max}} = 0.35$ represents an upper limit for a dust free homogeneous distribution of gas and sources. We derived its value as follows: Firstly we sum the Neufeld solutions (Eqn. 30) for an equidistant set of τ_0 values between $[0, \tau_0]$. Secondly, from the resulting Ly α line profile we estimate the effective τ_0^{eff} value by measuring the peak positions (x_p^{eff}). Relating these peak positions to those obtained for the single Neufeld solution for τ_0 (x_p), we obtain the ratio $x_p^{\text{eff}}/x_p = (\tau_0^{\text{eff}}/\tau_0)^{1/3} = (N_{\text{HI}}^{\text{eff}}/N_{\text{HI}})^{1/3}$, and the correction factor $\xi_{\text{max}} = (x_p^{\text{eff}}/x_p)^{1/3}$. We have also checked that applying the correction factor ξ to N_{HI} reproduces the correct shift in the Ly α peak positions x_p shown in Fig. A5 in [Forero-Romero et al. \(2011\)](#).

APPENDIX B: DELAYED NON-BURSTY SUPERNOVA FEEDBACK SCHEME

We briefly describe our new formalism for the number of SN exploding if the stellar mass formed in a time step is assumed to form at a continuous rate across that time step. For a given star formation history $\text{SFR}(t)$, the differential number of SN after a time t is given by

$$\frac{dN_{\text{SN}}}{dt}(t) = \int_0^\infty dt' \text{SFR}(t') \nu(t - t'). \quad (\text{B1})$$

$\nu(t)$ is the differential number of SN per stellar mass formed at $t' = 0$ and exploding at $t' = t$, and hence yields as

$$\nu(t) = M_{\text{SN}}^{-\gamma}(t) \frac{dM_{\text{SN}}}{dt} \Theta(t - t_{\star, \text{high}}) \Theta(t_{\text{SN}, \text{low}} - t), \quad (\text{B2})$$

with γ being the slope of the assumed IMF, $t_{\star, \text{high}}$ being the time after which the most massive stars sampled by the IMF, $M_{\star, \text{high}}$, explode as SN, and $t_{\text{SN}, \text{low}}$ the time that it takes a star with the lowest stellar mass to explode as SN ($M_{\text{SN}, \text{low}} = 8M_{\odot}$). Stars of mass M_{SN} explode after a time t and the corresponding relation is described by

$$\frac{M_{\text{SN}}}{M_{\odot}} = \left(\frac{t/\text{Myr} - 3}{1.2 \times 10^3} \right)^{-1/1.85} = a^{-c} (t - 3)^{-c}. \quad (\text{B3})$$

For constant star formation with

$$\text{SFR}(t) = \begin{cases} 0 & t < t_i \\ s_0 & t_i \leq t \leq t_f \\ 0 & t_f < t \end{cases} \quad (\text{B4})$$

we yield after inserting Eqn. B2 and B3 into Eqn. B1

$$\begin{aligned} \frac{dN_{\text{SN}}}{dt}(t) &= \int_{t_i}^{t_f} dt' s_0 \nu(t - t') \\ &= \int_{t_{\text{min}}}^{t_{\text{max}}} dt' s_0 M_{\text{SN}}^{-\gamma}(t - t') \frac{dM_{\text{SN}}}{d(t - t')} \\ &= - \int_{t_{\text{min}}}^{t_{\text{max}}} dt' s_0 c a^{c(\gamma-1)} (t - t' - 3)^{c(\gamma-1)-1} \\ &= s_0 \frac{a^{c(\gamma-1)}}{1 - \gamma} \\ &\times \left[(t - t_{\text{min}} - 3)^{c(\gamma-1)} - (t - t_{\text{max}} - 3)^{c(\gamma-1)} \right] \\ &= s_0 \frac{a^{c(\gamma-1)}}{1 - \gamma} [f_{\text{min}}(t) - f_{\text{max}}(t)] \end{aligned} \quad (\text{B5})$$

with

$$t_{\text{min}} = \max[t_i, t - t_{\text{SN}, \text{low}}] \quad (\text{B6})$$

$$t_{\text{max}} = \min[t_f, t - t_{\star, \text{high}}] \quad (\text{B7})$$

and

$$t_{\text{max}} \geq t_{\text{min}}. \quad (\text{B8})$$

These relations result in the following additional criteria

$$t \geq t_i + t_{\star, \text{high}} \quad (\text{B9})$$

$$t \leq t_f + t_{\text{SN}, \text{low}}. \quad (\text{B10})$$

Eqn. B6 describes the differential number of SN exploding between the onset of star formation (t_i) and time t assuming constant star formation from t_i to t_f . However, to obtain the total number of SN exploding in a given time step, i.e. between t_{j-1} and t_j , we need to integrate over all contributions from $t_{j-1} \leq t \leq t_j$ (i.e. integrating Eqn. B6 over time t),

$$\begin{aligned} N_{\text{SN}}(t_i, t_f, t_{j-1}, t_j) &= \int_{t_{j-1}}^{t_j} dt \frac{dN_{\text{SN}}}{dt} \\ &= \int_{t_{j-1}}^{t_j} dt s_0 \frac{a^{c(\gamma-1)}}{1 - \gamma} [f_{\text{min}}(t) - f_{\text{max}}(t)]. \end{aligned} \quad (\text{B11})$$

We solve the different summands in the integral separately, yielding

$$\begin{aligned} F_{\text{max}} &= \int_{t_{j-1}}^{t_j} dt f_{\text{max}}(t) \\ &= \int_{t_{j-1}}^{t_j} dt (t - t_{\text{max}} - 3)^{c(\gamma-1)} \\ &\times \Theta(t_f + t_{\text{SN}, \text{low}} - t) \Theta(t - t_i + t_{\star, \text{high}}) \\ &= \int_{\max(t_{j-1}, t_i + t_{\star, \text{high}})}^{\min(t_j, t_f + t_{\star, \text{high}})} dt (t_{\star, \text{high}} - 3)^{c(\gamma-1)} \\ &+ \int_{\max(t_{j-1}, t_f + t_{\star, \text{high}})}^{\min(t_j, t_f + t_{\text{SN}, \text{low}})} dt (t - t_f - 3)^{c(\gamma-1)} \\ &= \left[(t_{\star, \text{high}} - 3)^{c(\gamma-1)} t \right]_{\max(t_{j-1}, t_i + t_{\star, \text{high}})}^{\min(t_j, t_f + t_{\star, \text{high}})} \\ &+ \left[\frac{(t - t_f - 3)^{c(\gamma-1)+1}}{c(\gamma-1) + 1} \right]_{\max(t_{j-1}, t_f + t_{\star, \text{high}})}^{\min(t_j, t_f + t_{\text{SN}, \text{low}})} \end{aligned} \quad (\text{B12})$$

and

$$\begin{aligned}
 F_{\min} &= \int_{t_{j-1}}^{t_j} dt f_{\min}(t) & (B13) \\
 &= \int_{t_{j-1}}^{t_j} dt (t - t_{\min} - 3)^{c(\gamma-1)} \\
 &\quad \times \Theta(t_f + t_{\text{SN,low}} - t) \Theta(t - t_i + t_{\star,\text{high}}) \\
 &= \int_{\max(t_{j-1}, t_i + t_{\star,\text{high}})}^{\min(t_j, t_i + t_{\text{SN,low}})} dt (t - t_i - 3)^{c(\gamma-1)} \\
 &\quad + \int_{\max(t_{j-1}, t_i + t_{\text{SN,low}})}^{\min(t_j, t_f + t_{\text{SN,low}})} dt (t_{\text{SN,low}} - 3)^{c(\gamma-1)} \\
 &= \left[(t_{\star,\text{high}} - 3)^{c(\gamma-1)} t \right]_{\max(t_{j-1}, t_i + t_{\star,\text{high}})}^{\min(t_j, t_i + t_{\text{SN,low}})} \\
 &\quad + \left[\frac{(t - t_f - 3)^{c(\gamma-1)+1}}{c(\gamma-1) + 1} \right]_{\max(t_{j-1}, t_i + t_{\text{SN,low}})}^{\min(t_j, t_f + t_{\text{SN,low}})}.
 \end{aligned}$$

Inserting Eqn. B13 and B14 into Eqn. B12, we obtain

$$N_{\text{SN}}(t_i, t_f, t_{j-1}, t_j) = s_0 \frac{a^{c(\gamma-1)}}{1-\gamma} [F_{\min} - F_{\max}] \quad (B14)$$

For a given star formation law $\text{SFR}(t)$, the total stellar mass formed across all time is

$$\begin{aligned}
 M_{\star}^{\text{tot}} &= \int_0^{\infty} dt \text{SFR}(t) \left[\int_{M_{\star,\text{high}}}^{M_{\star,\text{low}}} dm m^{1-\gamma} \right] & (B15) \\
 &= \int_0^{\infty} dt \text{SFR}(t) \frac{M_{\star,\text{low}}^{2-\gamma} - M_{\star,\text{high}}^{2-\gamma}}{2-\gamma}.
 \end{aligned}$$

Hence, for a constant star formation between t_i and t_f , we finally obtain

$$M_{\star}^{\text{tot}}(t_i, t_f) = \frac{s_0}{t_f - t_i} \frac{M_{\star,\text{low}}^{2-\gamma} - M_{\star,\text{high}}^{2-\gamma}}{2-\gamma} \quad (B16)$$

Finally, from Eqn. B14 and B16, we derive the number of SN exploding between times t_{j-1} and t_j from stars formed between t_i and t_j per stellar mass as

$$\frac{N_{\text{SN}}(t_i, t_f, t_{j-1}, t_j)}{M_{\star}^{\text{tot}}(t_i, t_f)} = \frac{2-\gamma}{1-\gamma} \frac{a^{c(\gamma-1)}}{M_{\star,\text{low}}^{2-\gamma} - M_{\star,\text{high}}^{2-\gamma}} \frac{F_{\min} - F_{\max}}{t_f - t_i} \quad (B17)$$

This paper has been typeset from a $\text{\TeX}/\text{\LaTeX}$ file prepared by the author.